

This is an Open Access document downloaded from ORCA, Cardiff University's institutional repository: <https://orca.cardiff.ac.uk/id/eprint/115230/>

This is the author's version of a work that was submitted to / accepted for publication.

Citation for final published version:

Johnson, Luke A. , Robertson, Angus J., Baxter, Nicola J., Trevitt, Clare R., Bisson, Claudine, Jin, Yi , Wood, Henry P., Hounslow, Andrea M., Cliff, Matthew J., Blackburn, G. Michael, Bowler, Matthew W. and Waltho, Jonathan P. 2018. van der Waals contact between nucleophile and transferring phosphorus is insufficient to achieve enzyme transition-state architecture. *ACS Catalysis* 8 (9) , pp. 8140-8153.  
10.1021/acscatal.8b01612

Publishers page: <http://dx.doi.org/10.1021/acscatal.8b01612>

Please note:

Changes made as a result of publishing processes such as copy-editing, formatting and page numbers may not be reflected in this version. For the definitive version of this publication, please refer to the published source. You are advised to consult the publisher's version if you wish to cite this paper.

This version is being made available in accordance with publisher policies. See <http://orca.cf.ac.uk/policies.html> for usage policies. Copyright and moral rights for publications made available in ORCA are retained by the copyright holders.



1  
2  
3  
4 van der Waals contact between nucleophile and  
5  
6  
7  
8  
9 transferring phosphorus is insufficient to achieve  
10  
11  
12  
13 enzyme transition state architecture  
14  
15  
16  
17

18 *Luke A. Johnson,<sup>†,¥,#</sup>, Angus J. Robertson,<sup>†,#</sup> Nicola J. Baxter,<sup>†,‡</sup> Clare R. Trevitt,<sup>†</sup>*  
19  
20 *Claudine Bisson,<sup>†,§</sup> Yi Jin,<sup>†,¥</sup> Henry P. Wood,<sup>†</sup> Andrea M. Hounslow,<sup>†</sup> Matthew J. Cliff,<sup>‡</sup>*  
21  
22 *G. Michael Blackburn,<sup>†</sup> Matthew W. Bowler,<sup>||</sup> and Jonathan P. Waltho,<sup>†,‡,\*</sup>*  
23  
24  
25

26 <sup>†</sup> Krebs Institute for Biomolecular Research, Department of Molecular Biology and  
27  
28 Biotechnology, The University of Sheffield, Sheffield, S10 2TN, United Kingdom  
29  
30

31 <sup>‡</sup> Manchester Institute of Biotechnology and School of Chemistry, The University of Manchester,  
32  
33 Manchester, M1 7DN, United Kingdom  
34  
35

36  
37 <sup>||</sup> European Molecular Biology Laboratory, Grenoble Outstation, 71 avenue des Martyrs, CS  
38  
39 90181 F-38042 Grenoble, France  
40  
41  
42  
43  
44  
45  
46  
47  
48  
49  
50  
51  
52  
53  
54  
55  
56  
57  
58  
59  
60



## ABSTRACT

Phosphate plays a crucial role in biology, owing to the stability of the phosphate ester bond. To overcome this inherent stability, enzymes that catalyze phosphoryl transfer reactions achieve enormous rate accelerations to operate on biologically relevant timescales and the mechanisms that underpin catalysis have been the subject of extensive debate. In an archetypal system,  $\beta$ -phosphoglucomutase catalyzes the reversible isomerization of  $\beta$ -glucose 1-phosphate and glucose 6-phosphate *via* two phosphoryl transfer steps using a  $\beta$ -glucose 1,6-bisphosphate intermediate and a catalytic  $\text{Mg}^{\text{II}}$  ion. In the present work, a variant of  $\beta$ -phosphoglucomutase, where the aspartate residue that acts as a general acid-base is replaced with asparagine, traps highly stable complexes containing the  $\beta$ -glucose 1,6-bisphosphate intermediate in the active site. Crystal structures of these complexes show that, when the enzyme is unable to transfer a proton, the intermediate is arrested in catalysis at an initial stage of phosphoryl transfer. The nucleophilic oxygen and transferring phosphorus atoms are aligned and in van der Waals contact, yet the enzyme is less closed than in transition state (analogue) complexes and binding of the catalytic  $\text{Mg}^{\text{II}}$  ion is compromised. Together, these observations indicate that optimal closure and optimal  $\text{Mg}^{\text{II}}$  binding occur only at higher energy positions on the reaction trajectory, allowing the enzyme to balance efficient catalysis with product dissociation. It is also confirmed that the general acid-base ensures that mutase activity is  $\sim 10^3$  fold greater than phosphatase activity in  $\beta$ -phosphoglucomutase.

## KEYWORDS

phosphoryl transfer enzyme | general acid-base catalysis | near attack conformation | magnesium ion affinity | X-ray crystallography

## INTRODUCTION

The efficiency of phosphoryl transfer enzymes in overcoming the stability of phosphate mono- and di-esters under physiological conditions has enabled biology to perform a vast array of functions, spanning transient cell signaling cascades, energy storage and consumption, protein regulation and the manipulation of genetic material (1). Phosphoryl transfer enzymes can achieve catalytic rate constants ( $k_{\text{cat}}$ ) of greater than  $100 \text{ s}^{-1}$ , even when spontaneous rate constants are as low as  $10^{-20} \text{ s}^{-1}$ . As such, they possess some of the largest enzymatic accelerations identified, with catalytic enhancements approaching  $10^{21}$  (2). Part of these accelerations has often been ascribed to general acid-base catalysis that both augments phosphorylation rates by assisting deprotonation of the nucleophilic hydroxyl oxygen, and enhances dephosphorylation rates by aiding protonation of the same oxygen atom (now the bridging oxygen of the phosphate group). Residues that satisfy the assignment of the general acid-base (commonly aspartate, glutamate or histidine residues) are repeatedly conserved in the active sites of multiple superfamilies of phosphoryl transfer enzymes and are consistently identified by mutation studies as key elements of enzyme activity (3–8). While structural studies reveal the close proximity of the general acid-base to reacting groups in near-transition state complexes, the precise relationship of proton transfer to the mechanism of the phosphoryl transfer reaction remains uncertain. Density-functional theory (DFT) models of the phosphoryl transfer step in some enzymes predict that proton transfer occurs only when there is substantial bond formation between the hydroxyl nucleophile and the phosphorus atom (9–13), but conclusions based on DFT models depend on how closely the protein conformation reflects that in which proton transfer takes place. However, solvent deuterium isotope effect measurements and the pH dependence of pre-steady state kinetic analyses often support the DFT models in that the rate of phosphoryl transfer is interpreted to be

1  
2  
3 independent of hydroxyl nucleophile deprotonation (14–16). A resolution of the uncertainty over  
4  
5 how the proton transfer step contributes to the catalytic cycle requires direct structural evidence  
6  
7 of the protein conformation in which proton transfer occurs.  
8  
9

10  
11  
12  $\beta$ -phosphoglucomutase ( $\beta$ PGM) from *Lactococcus lactis* is a well-studied magnesium-  
13  
14 dependent phosphoryl transfer enzyme of the haloacid dehalogenase (HAD) superfamily (8,  
15  
16 17–23), which catalyzes the reversible isomerization of  $\beta$ -glucose 1-phosphate ( $\beta$ G1P) and  
17  
18 glucose 6-phosphate (G6P) (Figure 1A). The active site is located in the cleft formed between the  
19  
20 helical cap domain (T16–V87) and the  $\alpha/\beta$  core domain (M1–D15, S88–K216), with closure of  
21  
22 the cleft through domain reorientation occurring during catalysis. The active site binds two  
23  
24 phosphate groups, one in the *proximal* site adjacent to D8 and the catalytic  $\text{Mg}^{\text{II}}$  ion, and one in  
25  
26 the *distal* site ( $\sim 8$  Å away in the closed enzyme).  $\beta$ PGM transfers a phosphate group from the  
27  
28 phospho-enzyme ( $\beta\text{PGM}^{\text{P}}$ , phosphorylated on the carboxylate sidechain of residue D8) to the  
29  
30 physiological substrate,  $\beta$ G1P, (Step 1; (19)) forming an enzyme-bound  $\beta$ -glucose 1,6-  
31  
32 bisphosphate ( $\beta\text{G16BP}$ ) intermediate (18). Subsequent release of  $\beta\text{G16BP}$  to solution permits its  
33  
34 binding in the alternate orientation, leading to dephosphorylation of  $\beta\text{G16BP}$  (Step 2; (20)) and  
35  
36 the generation of G6P and  $\beta\text{PGM}^{\text{P}}$  as products (Figure 1A). In the Step 1 complexes,  $\beta$ PGM  
37  
38 hydrogen bonds to the substrate directly, whereas in the Step 2 complexes, two water molecules  
39  
40 mediate hydrogen bonding with substrate (19). Structural investigations of species along the  
41  
42 reaction coordinate have made extensive use of metal fluoride-based ground and transition state  
43  
44 analogue complexes (24, 25), and have experimentally corroborated the in-line nucleophilic  
45  
46 attack of phosphoryl transfer, the trigonal bipyramidal nature of the chemical transition state  
47  
48 (TS), and the requirement for charge balance in the active site (20–22). Moreover, these studies  
49  
50  
51  
52  
53  
54  
55  
56  
57  
58  
59  
60

1  
2  
3 have highlighted how the carboxylate group of the assigned general acid-base (residue D10) can  
4  
5 adopt different orientations (8). In substrate-free  $\beta$ PGM and  $\beta$ PGM<sup>P</sup> analogue structures (20,  
6  
7 23), the active site cleft is open and the D10 carboxylate is in the *out* position (Figure 1B). In  
8  
9 transition state analogue (TSA) structures (20), domain reorientation has closed the active site  
10  
11 cleft and the D10 carboxylate is in the *in* position, where it is positioned to facilitate general  
12  
13 acid-base catalysis. In the substrate-bound  $\beta$ PGM<sup>P</sup> analogue structures containing BeF<sub>3</sub><sup>-</sup> (23) two  
14  
15 conformations are observed, in both of which the active site cleft is closed. One has the same  
16  
17 conformation as the TSA structures, while in the other the cap and core domains have a relative  
18  
19 rotation of 17° and the D10 carboxylate is in the *out* position. Both of the substrate-bound  
20  
21  $\beta$ PGM<sup>P</sup> analogue structures conform to the criteria of near attack conformations (NACs) (26).  
22  
23 The TSA-like conformation is termed an aligned NAC as the nucleophile is aligned to attack the  
24  
25 BeF<sub>3</sub><sup>-</sup> moiety, whereas the rotated conformation is termed a hydrogen-bonded NAC as the  
26  
27 nucleophilic hydroxyl group is hydrogen bonded to the BeF<sub>3</sub><sup>-</sup> moiety (23). The observation of  
28  
29 both NACs supports a model where the conformational change between the two closed forms is  
30  
31 correlated with the *out* to *in* transition of D10 and the alignment of the substrate for nucleophilic  
32  
33 attack.  
34  
35  
36  
37  
38  
39  
40  
41  
42  
43  
44  
45  
46  
47  
48  
49  
50  
51  
52  
53  
54  
55  
56  
57  
58  
59  
60

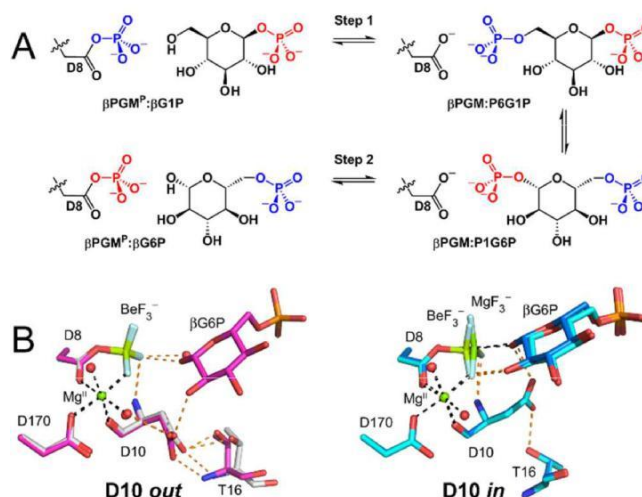


**Figure 1.** The  $\beta$ PGM reaction scheme and change in orientation of residue D10, the assigned general acid-base. (A)  $\beta$ PGM reaction scheme for the enzymatic conversion of  $\beta$ G1P to G6P via a  $\beta$ G16BP intermediate. The phosphoryl transfer reaction between the phospho-enzyme ( $\beta$ PGM<sup>P</sup>, phosphorylated at residue D8) and  $\beta$ G1P is termed Step 1 and is illustrated with the transferring phosphate (blue) in the *proximal* site and the 1-phosphate (red) of  $\beta$ G1P in the *distal* site. The equivalent reaction between  $\beta$ PGM<sup>P</sup> and G6P is termed Step 2 and is shown with the transferring phosphate (red) in the *proximal* site and the 6-phosphate (blue) of G6P in the *distal* site. The two intermediate complexes are labeled  $\beta$ PGM:P6G1P and  $\beta$ PGM:P1G6P to explicitly denote the orientation of  $\beta$ G16BP bound in the active site. (B) The carboxylate group of residue D10 is in the *out* position in both the open substrate-free  $\beta$ PGM<sup>P</sup> analogue structure ( $\beta$ PGM:BeF<sub>3</sub> complex; PDB 2WFA (23); gray carbon atoms) and in the hydrogen bonded NAC ( $\beta$ PGM:BeF<sub>3</sub>:G6P complex; PDB 2WF9 (23); magenta carbon atoms). In contrast, the carboxylate group of residue D10 is in the *in* position in both the transition state analogue (TSA) structure ( $\beta$ PGM:MgF<sub>3</sub>:G6P TSA complex; PDB 2WF5 (20); blue carbon atoms) and in the aligned NAC ( $\beta$ PGM:BeF<sub>3</sub>:G6P complex; PDB 2WF8 (23); cyan carbon atoms). Selected active



1  
2  
3 site residues and ligand are shown as sticks in standard CPK colors, with beryllium (light green),  
4  
5 magnesium (green) and fluorine (light blue). Structural waters (red) and the catalytic  $\text{Mg}^{\text{II}}$  ion  
6  
7 (green) are drawn as spheres. Orange dashes indicate hydrogen bonds and black dashes show  
8  
9 metal ion coordination.  
10

11  
12  
13  
14  
15 The models above require extrapolation from the behavior of metal fluoride analogues in the  
16  
17 active site to that of the substrates. While there is growing computational evidence for a close  
18  
19 relationship between metal fluoride TSA complexes and the corresponding phosphoryl species  
20  
21 (27, 28), there are few experimental systems where the properties of both species can be  
22  
23 examined in detail. In order to address this, we sought to establish a stable enzyme:substrate  
24  
25 complex using an aspartate to asparagine substitution, in a system for which the behavior of  
26  
27 metal fluoride analogue complexes is well determined (20, 23). Here, we report the properties of  
28  
29 several complexes involving the  $\beta\text{PGM D10N}$  variant ( $\beta\text{PGM}_{\text{D10N}}$ ), which serves as a model of  
30  
31 wild-type  $\beta\text{PGM}$  ( $\beta\text{PGM}_{\text{WT}}$ ) with the general acid-base in its protonated form. This variant has  
32  
33 previously been reported to be inactive (8), and was expected to offer the opportunity to study  
34  
35  $\beta\text{PGM}^{\text{P}}:\beta\text{G1P}$ ,  $\beta\text{PGM}^{\text{P}}:\text{G6P}$  and  $\beta\text{PGM}:\beta\text{G16BP}$  complexes independently. Here we show that  
36  
37 the  $\beta\text{PGM}_{\text{D10N}}$  variant purifies as  $\beta\text{PGM}_{\text{D10N}}:\beta\text{G16BP}$  complexes. Low-level mutase activity was  
38  
39 observed, which was enhanced once the non-covalently-bound intermediate is removed by  
40  
41 denaturation-refolding. Subsequently, exposure to substrate leads to the reformation of  
42  
43  $\beta\text{PGM}_{\text{D10N}}:\beta\text{G16BP}$  complexes in solution, and the trapping of two distinct  $\beta\text{PGM}_{\text{D10N}}:\beta\text{G16BP}$   
44  
45 complexes *in crystallo*, with either the 1- or the 6-phosphate group in the *proximal* site. In both  
46  
47 of these complexes, the nucleophilic carboxylate oxygen and the phosphorus atoms are aligned  
48  
49 and in van der Waals contact, but phosphoryl transfer is arrested by the failure of N10 to release  
50  
51  
52  
53  
54  
55  
56  
57  
58  
59  
60

1  
2  
3 a proton to  $\beta$ G16BP. However, the  $\beta$ PGM<sub>D10N</sub>: $\beta$ G16BP complexes do not adopt the fully closed  
4  
5 conformation of the TSA complexes, indicating that such close proximity between reacting groups is  
6  
7 insufficient to achieve the architecture used by the enzyme to bind the TS. Remarkably,  
8  
9 the binding affinity of the catalytic Mg<sup>II</sup> ion in the  $\beta$ PGM<sub>D10N</sub>: $\beta$ G16BP complexes is reduced  
10  
11 compared to the phospho-enzyme analogue and the TSA complexes, which implies that  
12  
13 antagonism within the coordination of the Mg<sup>II</sup> ion facilitates the release of the high affinity  
14  
15  $\beta$ G16BP intermediate.  
16  
17  
18  
19  
20  
21  
22

## 23 EXPERIMENTAL METHODS

24  
25  
26  **$\beta$ -Phosphoglucomutase ( $\beta$ PGM) expression, purification and refolding.** Site-directed  
27  
28 mutagenesis (QuikChange II kit, Agilent Technologies) of the  $\beta$ PGM gene from *Lactococcus*  
29  
30 *lactis* (EC 5.4.2.6) cloned in a pET22b+ vector was employed to generate the D10N variant  
31  
32 ( $\beta$ PGM<sub>D10N</sub>) and the D8N variant ( $\beta$ PGM<sub>D8N</sub>) using primers with single-site base changes and  
33  
34 mutagenesis of the  $\beta$ PGM gene was confirmed by DNA sequencing. Wild-type  $\beta$ PGM  
35  
36 ( $\beta$ PGM<sub>WT</sub>),  $\beta$ PGM<sub>D10N</sub> and  $\beta$ PGM<sub>D8N</sub> proteins were expressed using natural abundance, <sup>15</sup>N or  
37  
38 <sup>2</sup>H<sup>15</sup>N<sup>13</sup>C isotopic enrichment (21, 29) and purified using the following methodology which  
39  
40 minimized the presence of contaminating phosphoryl transfer enzymes (*e.g.*, phosphoglucose  
41  
42 isomerase and  $\beta$ PGM from *E. coli*). The cell pellet was resuspended in ice-cold standard native  
43  
44 buffer (50 mM K<sup>+</sup> HEPES (pH 7.2), 5 mM MgCl<sub>2</sub>, 2 mM NaN<sub>3</sub>) supplemented with one tablet of  
45  
46 cComplete™ protease inhibitor cocktail (Roche). The cell suspension was lysed on ice by  
47  
48 sonication for 5 cycles of pulsation for 20 s with 60 s cooling intervals. The cell lysate was then  
49  
50 separated by ultracentrifugation (Beckman Coulter Avanti centrifuge) at 24,000 rpm for 35 min  
51  
52  
53  
54  
55  
56  
57  
58  
59  
60

1  
2  
3 at 4 °C. The cleared cell lysate was filtered using a 0.2 μM syringe filter and loaded onto a  
4 DEAE-Sepharose fast flow ion-exchange column connected to an ÄKTA purification system  
5  
6 that had been washed previously with 1 column volume of 6 M guanidine hydrochloride, 1  
7  
8 column volume of 1 M NaOH and equilibrated with 5 column volumes of standard native buffer.  
9  
10 Following extensive washing, proteins bound to the DEAE-Sepharose column were eluted with a  
11  
12 gradient of 0 to 100% standard native buffer containing 0.5 M NaCl. Fractions containing βPGM  
13  
14 were checked for purity using SDS-PAGE, were pooled together and concentrated by Vivaspin  
15  
16 (10 kDa MWCO). The protein sample was filtered using a 0.2 μM syringe filter and loaded onto  
17  
18 a prepacked Hiload 26/60 Superdex 75 size-exclusion column connected to an ÄKTA  
19  
20 purification system that had been washed previously with 1 column volume of 1 M NaOH and  
21  
22 equilibrated with 5 column volumes of filtered and degassed standard native buffer containing 1  
23  
24 M NaCl. Fractions containing βPGM were checked for purity using SDS-PAGE, were pooled  
25  
26 together, buffer exchanged into standard native buffer and concentrated to 2 mM by Vivaspin  
27  
28 (10 kDa MWCO) for storage as 1 mL aliquots at -20 °C.  
29  
30  
31  
32  
33  
34  
35  
36

37 In contrast to βPGM<sub>WT</sub> and βPGM<sub>D8N</sub>, βPGM<sub>D10N</sub> co-purified with βG16BP as tight, non-  
38  
39 covalently bound βPGM<sub>D10N</sub>:βG16BP complexes. Substrate-free βPGM<sub>D10N</sub> was prepared from  
40  
41 the co-purified βPGM<sub>D10N</sub>:βG16BP complexes using an unfolding-dilution-refolding strategy to  
42  
43 remove βG16BP. Samples of the co-purified βPGM<sub>D10N</sub>:βG16BP complexes were diluted into  
44  
45 unfolding buffer (4 M guanidine hydrochloride, 50 mM K<sup>+</sup> HEPES (pH 7.2), 5 mM MgCl<sub>2</sub>, 2  
46  
47 mM NaN<sub>3</sub>), buffer exchanged by Vivaspin (10 kDa MWCO) in unfolding buffer to dilute  
48  
49 βG16BP by 200-fold, and the retained βPGM<sub>D10N</sub> was refolded by pulse renaturation or dialysis  
50  
51 into standard native buffer. A final buffer exchange to remove any remaining denaturant was  
52  
53  
54  
55  
56  
57  
58  
59  
60

1  
2  
3 performed using a Vivaspin (3 kDa MWCO) and the protein was concentrated to 2 mM for  
4 storage as 1 mL aliquots at  $-20\text{ }^{\circ}\text{C}$ . Removal of  $\beta\text{G16BP}$  from  $\beta\text{PGMD}_{10\text{N}}$  was confirmed by  $^{31}\text{P}$   
5  
6  
7 NMR spectroscopy in standard NMR buffer (50 mM  $\text{K}^+$  HEPES (pH 7.2), 5 mM  $\text{MgCl}_2$ , 2 mM  
8  
9  $\text{NaN}_3$ , 10% (v/v)  $^2\text{H}_2\text{O}$  and 1 mM trimethylsilyl propanoic acid (TSP)).

10  
11  
12 The reconstituted  $\beta\text{PGMD}_{10\text{N}}:\beta\text{G16BP}$  complexes were formed by the addition of 20 mM  
13  
14 acetyl phosphate (AcP) and 10 mM glucose 6-phosphate (G6P) or 10 mM  $\beta$ -glucose 1-phosphate  
15  
16 ( $\beta\text{G1P}$ ) to 1 mM substrate-free  $\beta\text{PGMD}_{10\text{N}}$  in 200 mM  $\text{K}^+$  HEPES buffer (pH 7.2), 5 mM  $\text{MgCl}_2$   
17  
18 and 2 mM  $\text{NaN}_3$ . Unbound ligands in the sample (excess G6P,  $\beta\text{G1P}$  and AcP) were removed by  
19  
20  
21  
22 buffer exchange into standard NMR buffer.

23  
24 **Reagents.** Unless otherwise stated, reagents were purchased from Sigma-Aldrich, GE  
25  
26 Healthcare, Melford Laboratories or CortecNet.

27  
28  
29  $\beta\text{G16BP}$  was isolated from the co-purified  $\beta\text{PGMD}_{10\text{N}}:\beta\text{G16BP}$  complexes in standard NMR  
30  
31 buffer by heat denaturation of  $\beta\text{PGMD}_{10\text{N}}$  (2 min at  $80\text{ }^{\circ}\text{C}$ ), centrifugation at 13,000 rpm to  
32  
33 remove denatured  $\beta\text{PGMD}_{10\text{N}}$  and filtration of the supernatant containing  $\beta\text{G16BP}$  using a  
34  
35 Vivaspin (3 kDa MWCO). Resonance assignments of  $\beta\text{G16BP}$  were confirmed by  $^{31}\text{P}$  and  
36  
37 natural abundance  $^1\text{H}^{13}\text{C}$  HSQC NMR spectra following the addition of 6 mM EDTA to the  
38  
39  
40  
41 sample.

42  
43  
44  $\beta\text{G1P}$  was synthesized enzymatically from maltose using maltose phosphorylase (EC 2.4.1.8).  
45  
46 1 M maltose was incubated overnight at  $30\text{ }^{\circ}\text{C}$  with  $1.5\text{ units mL}^{-1}$  maltose phosphorylase in 0.5  
47  
48 M phosphate buffer (pH 7.0).  $\beta\text{G1P}$  production was confirmed using  $^{31}\text{P}$  NMR spectroscopy.  
49  
50 Maltose phosphorylase (90 kDa) was removed using a Vivaspin (5 kDa MWCO) and the  
51  
52 resulting flow-through solution containing  $\beta\text{G1P}$  was used without further purification. The  
53  
54 concentration of  $\beta\text{G1P}$  was measured to be 150 mM by quantitative  $^{31}\text{P}$  NMR spectroscopy  
55  
56  
57  
58  
59  
60

1  
2  
3 (recycle time 60 s) against a known concentration of G6P. The concentrations of other  
4  
5 components in the solution were estimated as follows: 150 mM glucose, 850 mM maltose and  
6  
7 350 mM inorganic phosphate.  
8  
9

10 Uniformly  $^{13}\text{C}$ -labeled G6P was synthesized enzymatically from 45 mM uniformly  $^{13}\text{C}$ -labeled  
11  
12 D-glucose by incubation for 90 min at 37 °C with 14 units  $\text{mL}^{-1}$  hexokinase (EC 2.7.1.1) and 50  
13  
14 mM ATP in 100 mM Tris-HCl (pH 8.0), 50 mM  $\text{MgCl}_2$  and 2 mM EDTA. G6P production was  
15  
16 confirmed using  $^{31}\text{P}$  NMR spectroscopy. Hexokinase (110 kDa) was removed by denaturation at  
17  
18 80 °C followed by filtration using a Vivaspin (3 kDa MWCO). The flow-through containing  
19  
20 uniformly  $^{13}\text{C}$ -labeled G6P was used without further purification together with AcP and  
21  
22 substrate-free  $\beta\text{PGMD}_{10\text{N}}$  for the formation of uniformly  $^{13}\text{C}$ -labeled  $\beta\text{G16BP}$  in the reconstituted  
23  
24  $\beta\text{PGMD}_{10\text{N}}:\beta\text{G16BP}$  complexes.  
25  
26  
27  
28

29 Chemically synthesized  $\beta\text{G16BP}$  was a gift from Prof. Nicholas Williams, Department of  
30  
31 Chemistry, The University of Sheffield (30).  
32  
33

### 34 **NMR spectroscopy.**

35  
36 **Instruments and data processing.** NMR experiments were acquired at 298 K using Bruker  
37  
38 spectrometers located at the following institutions: Department of Molecular Biology and  
39  
40 Biotechnology (MBB), The University of Sheffield; School of Chemistry (SC), The University  
41  
42 of Manchester; Manchester Institute of Biotechnology (MIB), The University of Manchester.  
43  
44 Experiments were processed using TopSpin (Bruker) or FELIX (Felix NMR, Inc.) and figures  
45  
46 were prepared using either FELIX or CcpNmr Analysis (31).  $^1\text{H}$  chemical shifts were referenced  
47  
48 relative to the internal TSP signal resonating at 0.0 ppm and  $^{13}\text{C}$ ,  $^{15}\text{N}$  and  $^{31}\text{P}$  chemical shifts  
49  
50 were referenced indirectly using nuclei-specific gyromagnetic ratios.  
51  
52  
53  
54  
55  
56  
57  
58  
59  
60

1  
2  
3  **$^1\text{H}^{15}\text{N}$  TROSY spectra.**  $^1\text{H}^{15}\text{N}$  TROSY spectra of  $\beta\text{PGM}_{\text{WT}}$  and substrate-free  $\beta\text{PGM}_{\text{D10N}}$   
4  
5 were acquired using 0.5 – 1 mM  $^{15}\text{N}$ - $\beta\text{PGM}$  in standard NMR buffer (50 mM  $\text{K}^+$  HEPES (pH  
6  
7 7.2), 5 mM  $\text{MgCl}_2$ , 2 mM  $\text{NaN}_3$  with 10% (v/v)  $^2\text{H}_2\text{O}$  and 2 mM TSP) containing 50 mM  $\text{MgCl}_2$ .  
8  
9  $^1\text{H}^{15}\text{N}$  TROSY spectra of the  $\beta\text{PGM}_{\text{WT}}:\text{BeF}_3$  and  $\beta\text{PGM}_{\text{D10N}}:\text{BeF}_3$  complexes were acquired  
10  
11 using 0.5 – 1 mM  $^{15}\text{N}$ - $\beta\text{PGM}_{\text{WT}}$  or  $^{15}\text{N}$ -substrate-free  $\beta\text{PGM}_{\text{D10N}}$  in standard NMR buffer  
12  
13 containing 5 mM  $\text{BeCl}_2$  and 10 mM  $\text{NH}_4\text{F}$ . Experiments were recorded using a Bruker 600 MHz  
14  
15 Avance DRX spectrometer equipped with a TXI cryoprobe and z-axis gradients (MBB) or a  
16  
17 Bruker 800 MHz Avance I spectrometer equipped with a TXI probe and z-axis gradients (MBB).  
18  
19

20  
21  
22  **$^{31}\text{P}$  spectra.** One-dimensional  $^{31}\text{P}$  spectra to characterize  $\beta\text{G16BP}$  and the  $\beta\text{PGM}_{\text{D10N}}:\beta\text{G16BP}$   
23  
24 complexes were acquired using a Bruker 500 MHz Avance DRX spectrometer (operating at  
25  
26 202.456 MHz for  $^{31}\text{P}$ ) equipped with a broadband probe (MBB). A spectral width of 50 ppm  
27  
28 centered at -10 ppm enabled the observation of the relevant phosphorus signals. Typically,  
29  
30 accumulations of 10,000 transients without proton-phosphorus decoupling were necessary to  
31  
32 achieve a sufficient signal-to-noise ratio with sample concentrations in the 0.5 – 1 mM range.  
33  
34 Spectra were processed with baseline correction and 10 Hz Lorentzian apodization.  
35  
36  
37

38  
39  **$^{31}\text{P}$  spectra for kinetic measurements.** Reaction kinetics for  $\beta\text{PGM}$ -catalyzed reactions were  
40  
41 followed using a Bruker 500 MHz Avance III HD spectrometer (operating at 202.48 MHz for  
42  
43  $^{31}\text{P}$ ) equipped with a Prodigy BBO cryoprobe (SC), which offered significant improvements in  
44  
45 signal sensitivity. One-dimensional  $^{31}\text{P}$  spectra without proton-phosphorus decoupling were  
46  
47 recorded within 1 minute, with 16 transients and a 2 s recycle delay to give signal-to-noise ratios  
48  
49 for 10 mM  $\beta\text{G1P}$  of greater than 100:1. The equilibrations of 10 mM  $\beta\text{G1P}$  with G6P by 0.1 – 1  
50  
51  $\mu\text{M}$   $\beta\text{PGM}_{\text{WT}}$ , 5 – 50  $\mu\text{M}$  substrate-free  $\beta\text{PGM}_{\text{D10N}}$  and 10  $\mu\text{M}$   $\beta\text{PGM}_{\text{D8N}}$  were measured in  
52  
53 standard kinetic buffer (200 mM  $\text{K}^+$  HEPES buffer (pH 7.2), 5 mM  $\text{MgCl}_2$ , 2 mM  $\text{NaN}_3$ , 10%  
54  
55  
56  
57  
58  
59  
60

1  
2  
3  $^2\text{H}_2\text{O}$  and 2 mM TSP). The reaction was initiated by and timed from the addition of 20 mM AcP  
4  
5 and monitored by the acquisition of consecutive  $^{31}\text{P}$  spectra. The equilibration of 10 mM  $\beta\text{G1P}$   
6  
7 with G6P by 5  $\mu\text{M}$  substrate-free  $\beta\text{PGM}_{\text{D10N}}$  using  $\beta\text{G16BP}$  extracted from the co-purified  
8  
9  $\beta\text{PGM}_{\text{D10N}}:\beta\text{G16BP}$  complexes as a priming agent was measured in standard kinetic buffer  
10  
11 monitored by one-dimensional  $^{31}\text{P}$  spectra recorded without proton-phosphorus decoupling with  
12  
13 256 transients and a 1 s recycle delay using a Bruker 500 MHz Avance DRX spectrometer  
14  
15 (MBB). Normalized integral values of both the  $\beta\text{G1P}$  and G6P peaks following baseline  
16  
17 correction and 2 Hz Lorentzian apodization were plotted against time to give kinetic profiles.  
18  
19 The linear steady-state portion of the G6P integral data was fitted using a linear least-squares  
20  
21 fitting algorithm to derive the catalytic rate constant,  $k_{\text{cat}}$ . The hydrolysis kinetics of 50 mM AcP  
22  
23 to inorganic phosphate and acetate by 250  $\mu\text{M}$   $\beta\text{PGM}$  was measured in standard kinetic buffer  
24  
25 containing 50 mM  $\text{MgCl}_2$  and 1 mM EDTA. The reaction was timed from the addition of AcP  
26  
27 and monitored by the acquisition of consecutive  $^{31}\text{P}$  spectra. Normalized integral values of the  
28  
29 AcP peak following baseline correction and 2 Hz Lorentzian apodization were plotted against  
30  
31 time and the rate constant for AcP hydrolysis was derived from linear least-squares fitting of the  
32  
33 data. A control experiment involving 50 mM AcP alone in standard kinetic buffer established  
34  
35 that hydrolysis of AcP was insignificant over the same timeframe. Throughout all the kinetic  
36  
37 measurements, the pH of the reactions was found to be invariant as assessed *in situ* by the  $^{31}\text{P}$   
38  
39 resonance of inorganic phosphate and the  $^1\text{H}$  resonances of 200 mM HEPES buffer.  
40  
41  
42  
43  
44  
45  
46

47  **$^1\text{H}^{13}\text{C}$  HSQC and 2D CCH-TOCSY spectra of glucose 1,6-bisphosphate species.** Natural  
48  
49 abundance  $^1\text{H}^{13}\text{C}$  HSQC spectra of  $\alpha\text{G16BP}$  and  $\beta\text{G16BP}$  (in 100%  $^2\text{H}_2\text{O}$  and 1 mM TSP) were  
50  
51 recorded on a Bruker 500 MHz Avance DRX spectrometer equipped with a TXI probe and z-  
52  
53 axis gradients (MBB) (30). To assign the bound  $\beta\text{G16BP}$  resonances in the reconstituted  
54  
55  
56  
57  
58  
59  
60

1  
2  
3  $\beta$ PGMD<sub>10N</sub>: $\beta$ G16BP complexes,  $^1\text{H}^{13}\text{C}$  HSQC and 2D CCH-TOCSY spectra were acquired with  
4  
5 0.5 – 1 mM  $^{15}\text{N}$ -labeled substrate-free  $\beta$ PGMD<sub>10N</sub> in standard NMR buffer containing 20 mM  
6  
7 AcP and 10 mM uniformly  $^{13}\text{C}$ -labeled G6P using a Bruker Avance III 800 MHz spectrometer  
8  
9 equipped with a TCI cryoprobe and z-axis gradients (MIB).  
10  
11

12  **$^1\text{H}^{15}\text{N}$  BEST-TROSY experiments.** Rapid acquisition  $^1\text{H}^{15}\text{N}$  BEST-TROSY spectra (32, 33) to  
13  
14 follow  $\beta$ PGMD<sub>10N</sub>-catalyzed reactions were acquired using 1 mM substrate-free  $\beta$ PGMD<sub>10N</sub> in  
15  
16 standard kinetic buffer containing either 20 mM AcP or 20 mM AcP and 10 mM  $\beta$ G1P.  $^1\text{H}^{15}\text{N}$   
17  
18 BEST-TROSY spectra were recorded using a Bruker 600 MHz Avance DRX spectrometer  
19  
20 equipped with a TXI cryoprobe and z-axis gradients (MBB) as 6 minute experiments (4  
21  
22 transients, 200 increments and a recycle delay of 0.3 s) with selective  $^1\text{H}$  pulses centered on the  
23  
24 amide region (8.7 ppm). Excitation pulses ( $90^\circ$ ) were 2 ms at 600 MHz (pulse shape Pc9\_4) and  
25  
26 1.7 ms at 600 MHz (pulse shape Eburp2), whereas refocusing pulses ( $180^\circ$ ) were 1.6 ms at 600  
27  
28 MHz (pulse shape Reburp). The experimental dead-time was approximately 6 minutes.  
29  
30  
31

32  
33 **Backbone resonance assignment of the  $\beta$ PGMD<sub>10N</sub>: $\beta$ G16BP complexes.** For the  $^1\text{H}$ ,  $^{13}\text{C}$   
34  
35 and  $^{15}\text{N}$  backbone resonance assignment of the reconstituted  $\beta$ PGMD<sub>10N</sub>: $\beta$ G16BP complexes,  
36  
37 multi-dimensional heteronuclear NMR spectra were acquired with 0.5 – 1 mM  $^2\text{H}^{15}\text{N}^{13}\text{C}$ -labeled  
38  
39 substrate-free  $\beta$ PGMD<sub>10N</sub> in standard NMR buffer containing 20 mM AcP and 10 mM G6P using  
40  
41 a Bruker 800 MHz Avance III spectrometer equipped with a TCI cryoprobe and z-axis gradients  
42  
43 (MIB). The standard suite of  $^1\text{H}^{15}\text{N}$ -TROSY and 3D TROSY-based constant time experiments  
44  
45 were acquired (HNCO, HN(CA)CO, HNCA, HN(CO)CA, HNCACB, HN(CO)CACB) using  
46  
47 non-uniform sampling (NUS) with a multi-dimensional Poisson Gap scheduling strategy with  
48  
49 exponential weighting (34). NUS data were reconstructed using TopSpin3 and multidimensional  
50  
51 decomposition (35). Backbone resonance assignments of the  $\text{Mg}^{\text{II}}$ -bound  $\beta$ PGMD<sub>10N</sub>:P1G6P and  
52  
53  
54  
55  
56  
57  
58  
59  
60



1  
2  
3 Mg<sup>II</sup>-free  $\beta$ PGM<sub>D10N</sub>:P1G6P complexes present simultaneously in the spectra were obtained  
4  
5 using a simulated annealing algorithm employed by the *asstools* assignment program (29).  
6

7  
8 Assignments for the two complexes were confirmed by using <sup>1</sup>H<sup>15</sup>N TROSY spectra of separate  
9  
10 Mg<sup>II</sup>-bound and Mg<sup>II</sup>-free <sup>15</sup>N- $\beta$ PGM<sub>D10N</sub>:P1G6P complexes, together with sequential backbone  
11  
12 amide to amide correlations obtained from TROSY-based (H)N(COCA)NNH and  
13  
14 H(NCOCA)NNH experiments (36). The Mg<sup>II</sup>-free <sup>15</sup>N- $\beta$ PGM<sub>D10N</sub>:P1G6P complex was prepared  
15  
16 by dilution of Mg<sup>II</sup> by over 20,000 fold using buffer exchange into standard NMR buffer in the  
17  
18 absence of MgCl<sub>2</sub>, while the Mg<sup>II</sup>-bound <sup>15</sup>N- $\beta$ PGM<sub>D10N</sub>:P1G6P complex was prepared in  
19  
20 standard NMR buffer containing 50 mM MgCl<sub>2</sub>.  
21  
22  
23

24  
25 **Determination of the Mg<sup>II</sup> dissociation constant.** A Mg<sup>II</sup>-free <sup>15</sup>N- $\beta$ PGM<sub>D10N</sub>: $\beta$ G16BP  
26  
27 complex was prepared from a reconstituted Mg<sup>II</sup>-bound <sup>15</sup>N- $\beta$ PGM<sub>D10N</sub>: $\beta$ G16BP complex by  
28  
29 buffer exchange (3000-fold dilution) and overnight equilibration into standard NMR buffer. A  
30  
31 discontinuous titration of 0 – 47.6 mM MgCl<sub>2</sub> into separate Mg<sup>II</sup>-free <sup>15</sup>N- $\beta$ PGM<sub>D10N</sub>: $\beta$ G16BP  
32  
33 samples with overnight equilibration was monitored by <sup>1</sup>H<sup>15</sup>N TROSY spectra recorded using a  
34  
35 Bruker 800 MHz Avance I spectrometer equipped with a TXI probe and z-axis gradients (MBB).  
36  
37 Peak intensities for well-resolved resonances of the Mg<sup>II</sup>-bound  $\beta$ PGM<sub>D10N</sub>: $\beta$ G16BP complex  
38  
39 (residues N10, G11, A115, K117 and I150) were averaged and normalized against the intensity  
40  
41 of the sidechain N $\epsilon$ 1 resonance of W216, which remains unchanged throughout the titration. The  
42  
43 dissociation constant (*K<sub>d</sub>*) was obtained by fitting changes in normalized peak intensity as a  
44  
45 function of Mg<sup>II</sup> concentration to a single-site binding isotherm (37) using a non-linear least  
46  
47 squares fitting algorithm. The solution concentration of Mg<sup>II</sup> present at the beginning of the  
48  
49 titration was derived from the fitting procedure.  
50  
51  
52  
53  
54

55 **X-ray crystallography.**  
56  
57  
58  
59  
60

1  
2  
3 **Crystallization and data collection.** Frozen aliquots of substrate-free  $\beta$ PGM<sub>D10N</sub> or co-  
4 purified  $\beta$ PGM<sub>D10N</sub>: $\beta$ G16BP complex in standard native buffer (50 mM K<sup>+</sup> HEPES (pH 7.2), 5  
5 mM MgCl<sub>2</sub>, 2 mM NaN<sub>3</sub>) were thawed on ice and centrifuged briefly to pellet insoluble material.  
6 Specific ligands were added to a solution of substrate-free  $\beta$ PGM<sub>D10N</sub> to generate crystals of the  
7 following complexes:  $\beta$ PGM<sub>D10N</sub>:BeF<sub>3</sub> complex (5 mM BeCl<sub>2</sub> and 15 mM NaF),  
8  $\beta$ PGM<sub>D10N</sub>:P1G6P and  $\beta$ PGM<sub>D10N</sub>:P6G1P complexes (15 mM  $\beta$ G1P, 5 mM BeCl<sub>2</sub> and 15 mM  
9 NaF) and  $\beta$ PGM<sub>D10N</sub>:AlF<sub>4</sub>:G6P complex (10 mM G6P, 5 mM AlCl<sub>3</sub> and 20 mM NaF). Crystals  
10 of the  $\beta$ PGM<sub>D10N</sub>:AlF<sub>4</sub>:H<sub>2</sub>O: $\beta$ G1P complex were obtained from a solution of the co-purified  
11  $\beta$ PGM<sub>D10N</sub>: $\beta$ G16BP complexes containing 5 mM  $\beta$ G1P, 2 mM AlCl<sub>3</sub> and 10 mM NH<sub>4</sub>F. Crystals  
12 of the co-purified  $\beta$ PGM<sub>D10N</sub>:P1G6P complex were obtained from a solution of the co-purified  
13  $\beta$ PGM<sub>D10N</sub>: $\beta$ G16BP complexes. The solutions were adjusted to a protein concentration of 0.6  
14 mM, were incubated for 1 h and mixed 1:1 with precipitant (24 – 34% (w/v) PEG 4000 or 19 –  
15 21% (w/v) PEG 3350, 50 – 200 mM Na acetate and 0 – 100 mM Tris (pH 7.5)). Crystals were  
16 grown at 290 K by hanging-drop vapor diffusion using a 2  $\mu$ L drop suspended on a siliconized  
17 glass cover slip above a 700  $\mu$ L well. Thin plate, small needle or rod shaped crystals grew  
18 typically over several days. Crystals were harvested using a mounted LithoLoop (Molecular  
19 Dimensions Ltd.) and were either cryo-protected in their mother liquor containing an additional  
20 25% (v/v) ethylene glycol or excess mother liquor was removed (38) prior to plunging into liquid  
21 nitrogen. Diffraction data were collected at 100 K on the MX beamlines at the Diamond Light  
22 Source (DLS), Oxfordshire, United Kingdom and on beamline ID14-2 at the European  
23 Synchrotron Radiation Facility (ESRF), Grenoble, France.

24  
25  
26  
27  
28  
29  
30  
31  
32  
33  
34  
35  
36  
37  
38  
39  
40  
41  
42  
43  
44  
45  
46  
47  
48  
49  
50  
51  
52  
53 **Data processing, structural determination and refinement.** At the DLS, data were  
54 processed using the xia2 pipeline (39), whereas at the ESRF, data were processed with  
55  
56  
57  
58  
59  
60

1  
2  
3 iMOSFLM (40). Resolution cut-offs were applied using either CC-half or by consideration of the  
4  
5  $\langle I/\sigma(I) \rangle$  and  $R_{\text{merge}}$  values. All the crystals belonged to the spacegroup  $P2_12_12_1$ , with cell  
6  
7 dimensions that varied depending on the degree of enzyme closure. Structures were determined  
8  
9 by molecular replacement with MolRep (41) using the highest resolution model with the most  
10  
11 appropriate cap and core domain relationship as a search model. Model building was carried out  
12  
13 in COOT (42) with ligands not included until the final rounds of refinement using REFMAC5  
14  
15 (43) so that they could be built into unbiased difference Fourier maps. When structures were  
16  
17 refined with down-weighted B-factor restraints, the B-factors of the ligands in the resulting  
18  
19 structures were equivalent to those of the surrounding protein, suggesting that the degree of  
20  
21 accuracy in the placement of the ligand atoms was equivalent to those of the protein atoms.  
22  
23 Structures with a resolution better than 1.4 Å were refined with anisotropic B-factors. Structure  
24  
25 validation was carried out in COOT and MolProbity (44). Superpositions were carried out using  
26  
27 PyMOL (45), maps were generated using FFT (46), and domain movements were calculated  
28  
29 using DynDom (47). Additional details for X-ray crystallography data collection, data processing  
30  
31 and refinement are provided in Table S1 in the Supporting Information.

32  
33  
34  
35  
36  
37  
38 **Crystallization of the  $\beta$ PGMD10N:P1G6P and the  $\beta$ PGMD10N:P6G1P complexes.** Rod  
39  
40 shaped crystals harvested after 1 week contained predominantly  $\beta$ G16BP in the  $\beta$ PGMD10N  
41  
42 active site, with the 6-phosphate group located in the *proximal* site and the 1-phosphate group  
43  
44 bound in the *distal* site ( $\beta$ PGMD10N:P6G1P complex). After refinement, the ratio of  $2F_o - F_c$   
45  
46 contour thresholds between the 1- and 6-phosphate groups (*ca.*  $6\sigma$  and  $5\sigma$ , respectively) did not  
47  
48 correlate with a full  $\beta$ G16BP ligand occupancy in the  $\beta$ PGMD10N:P6G1P complex. When  
49  
50 modeled at a ligand occupancy of 0.8, B-factor convergence was attained between the  $\beta$ G16BP  
51  
52 ligand and neighboring residues in the active site, confirming  $\beta$ G16BP as the dominant ligand.  
53  
54  
55  
56  
57  
58  
59  
60

1  
2  
3 Remaining difference map peaks were consistent with the presence of a minor population of  
4  
5  $\beta$ G1P (with the 1-phosphate in the *distal* site) but, due to poor connectivity at this resolution,  
6  
7  $\beta$ G1P was not modeled into the structure. Crystals from the same drop with the same  
8  
9 morphology harvested after 12 weeks contained only  $\beta$ G16BP bound in the alternate orientation  
10  
11 with the 1-phosphate group located in the *proximal* site and the 6-phosphate group bound in the  
12  
13 *distal* site ( $\beta$ PGM<sub>D10N</sub>:P1G6P complex).  
14  
15

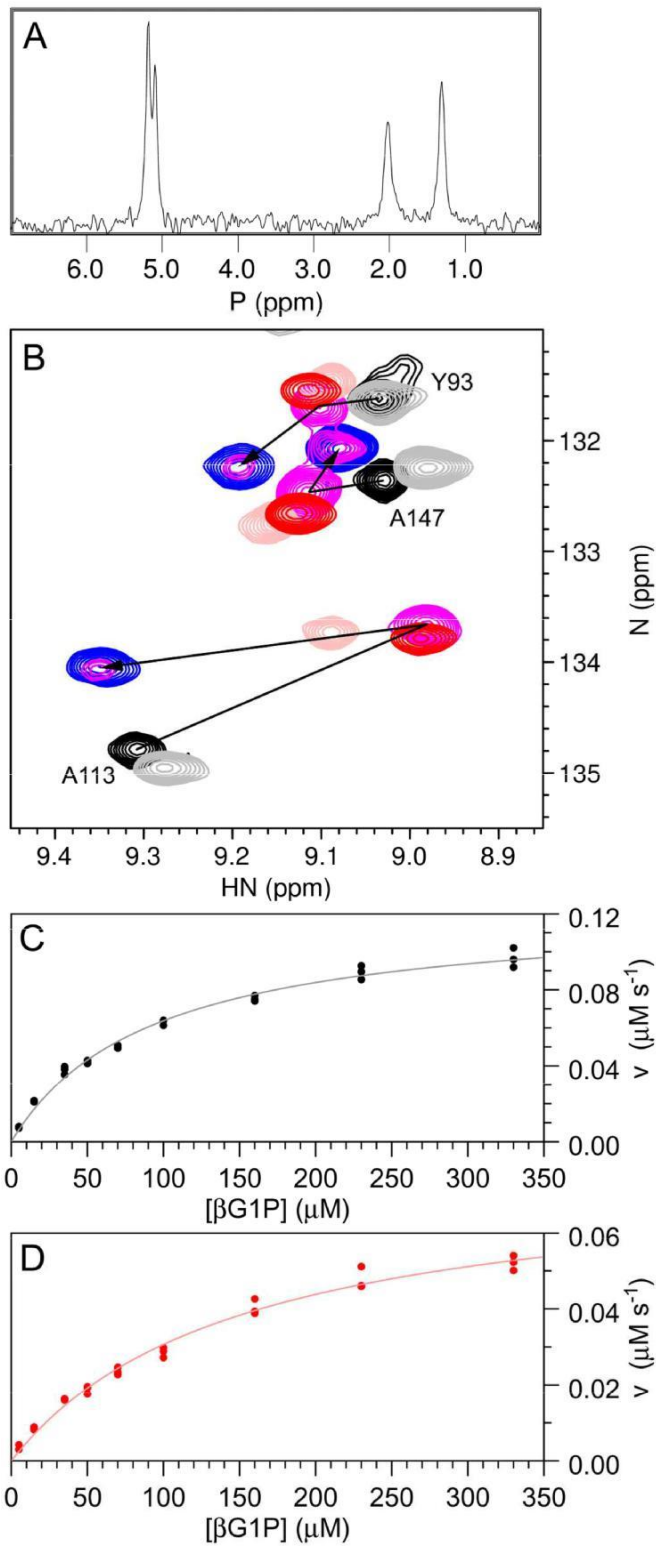
16  
17 **Steady-state kinetic assays.** Steady-state kinetic assays for  $\beta$ PGM<sub>WT</sub> and substrate-free  
18  
19  $\beta$ PGM<sub>D10N</sub> were conducted at 294 K using a FLUOstar OMEGA microplate reader (BMG  
20  
21 Labtech) in 200 mM K<sup>+</sup> HEPES buffer (pH 7.2) containing 5 mM MgCl<sub>2</sub> and 1 mM NaN<sub>3</sub> in a  
22  
23 200  $\mu$ L reaction volume. The rate of G6P production was measured indirectly using a glucose 6-  
24  
25 phosphate dehydrogenase (G6PDH) coupled assay, in which G6P is oxidized and concomitant  
26  
27 NAD<sup>+</sup> reduction is monitored by the increase in absorbance at 340 nm (NADH extinction  
28  
29 coefficient = 6220 M<sup>-1</sup> cm<sup>-1</sup>).  $\beta$ PGM<sub>WT</sub> and substrate-free  $\beta$ PGM<sub>D10N</sub> stock concentrations were  
30  
31 determined using a NanoDrop One<sup>C</sup> spectrophotometer (Thermo Scientific) and diluted  
32  
33 accordingly ( $\beta$ PGM extinction coefficient = 19940 M<sup>-1</sup> cm<sup>-1</sup>). For the determination of  $k_{cat}$  and  
34  
35  $K_m$  values, the reaction was initiated by the addition of 10 mM AcP to solutions of 0.5 mM  
36  
37 NAD<sup>+</sup> and 5 units mL<sup>-1</sup> G6PDH containing either 5 nM  $\beta$ PGM<sub>WT</sub> or 500 nM substrate-free  
38  
39  $\beta$ PGM<sub>D10N</sub> and variable concentrations of  $\beta$ G1P (5, 15, 35, 50, 70, 100, 160, 230, 330  $\mu$ M). The  
40  
41 linear steady-state portion of G6P production was fitted using a linear least-squares fitting algorithm  
42  
43 to determine the reaction velocity ( $v$ ) at each  $\beta$ G1P concentration. Data were subsequently fitted to  
44  
45 the standard Michaelis-Menten equation to derive  $k_{cat}$  and  $K_m$  values using  
46  
47 an in-house python non-linear least-squares fitting algorithm. Errors were estimated using a  
48  
49 python bootstrap resampling protocol and are presented at one standard deviation. For the  
50  
51  
52  
53  
54  
55  
56  
57  
58  
59  
60

1  
2  
3 fluoride inhibition experiments monitored using the G6PDH coupled assay, the reaction was  
4  
5 initiated by the addition of 10 mM AcP to solutions of 230  $\mu\text{M}$   $\beta\text{G1P}$ , 0.5 mM  $\text{NAD}^+$  and 5 units  
6  
7  $\text{mL}^{-1}$  G6PDH containing either 5 nM  $\beta\text{PGM}_{\text{WT}}$  or 500 nM substrate-free  $\beta\text{PGM}_{\text{D10N}}$  and variable  
8  
9 concentrations of NaF (0, 1, 2, 3, 5, 7, 10 mM). The linear steady-state portion of G6P  
10  
11 production was not used for the analysis of fluoride inhibition as  $\beta\text{G16BP}$  formation during the  
12  
13 reaction outcompetes fluoride inhibition (21). The presence of increasing levels of fluoride in the  
14  
15 reaction buffer extends the lag phase prior to achieving steady-state kinetics, the duration of  
16  
17 which was estimated using a first derivative approach. The time point at which the maximum  
18  
19 value was reached in the first derivative vs time plot for each reaction containing fluoride was  
20  
21 normalized against the time point for the reaction in the absence of fluoride. A line of best fit for  
22  
23 the normalized values vs fluoride concentration was determined using a polynomial function.  
24  
25  
26  
27  
28  
29  
30  
31

## 32 RESULTS

33  
34  
35 **Recombinant  $\beta\text{PGM}_{\text{D10N}}$  co-purifies in complex with  $\beta\text{G16BP}$ .**  $\beta\text{PGM}_{\text{D10N}}$  was produced  
36  
37 and purified as for  $\beta\text{PGM}_{\text{WT}}$  with slight modifications to published procedures (48–50). A  $^{31}\text{P}$   
38  
39 NMR spectrum demonstrated that, unlike  $\beta\text{PGM}_{\text{WT}}$ ,  $\beta\text{PGM}_{\text{D10N}}$  co-purifies with tightly-bound  
40  
41 phosphorylated glucose ligands (Figure 2A). Four  $^{31}\text{P}$  resonances are observed, two with  
42  
43 chemical shifts corresponding to a 1-phosphate group and two to a 6-phosphate group of glucose.  
44  
45 The ratio of intensities of the resonances suggests that the phosphate groups are paired,  
46  
47 consistent with the population of two complexes. Ligand extraction was achieved by the removal  
48  
49 of heat denatured  $\beta\text{PGM}_{\text{D10N}}$  (2 min at 80 °C) using centrifugation followed by membrane  
50  
51 filtration of the supernatant.  $^{31}\text{P}$  and  $^1\text{H}^{13}\text{C}$  HSQC NMR spectra indicated that a single ligand had  
52  
53  
54  
55  
56  
57  
58  
59  
60

1  
2  
3 been isolated, which revealed that both complexes contained the same phosphorylated glucose  
4 species (Figure S1 A, C and D and Figure S2B in the Supporting Information). The ligand was  
5 identified as  $\beta$ G16BP (the reaction intermediate, Figure 1A) by comparison with synthetic  $\alpha$ -and  
6  $\beta$ -glucose 1,6-bisphosphate species (Figure S1E and Figure S2A). The high affinity of  
7  $\beta$ PGM<sub>D10N</sub> for the  $\beta$ G16BP intermediate is predictable, since kinetic data for  $\beta$ PGM<sub>WT</sub> has  
8 identified that  $\beta$ G16BP is the tightest binding species of the native substrates, with  $K_m = 0.63 \mu\text{M}$   
9 (8) and  $K_m = 0.72 \mu\text{M}$  (30). Substitution of aspartate with asparagine at residue 10 is likely to  
10 increase the binding affinity of  $\beta$ PGM<sub>D10N</sub> for  $\beta$ G16BP since the deprotonated D10 sidechain in  
11  $\beta$ PGM<sub>WT</sub> does not satisfy charge balance (24) within the complex. Substrate-free  $\beta$ PGM<sub>D10N</sub> was  
12 prepared from the co-purified  $\beta$ PGM<sub>D10N</sub>: $\beta$ G16BP complexes by unfolding the recombinant  
13 protein in 4 M guanidine hydrochloride together with a 200-fold dilution of the ligand using  
14 buffer exchange and subsequent refolding of  $\beta$ PGM<sub>D10N</sub> (Figure S1B). A comparison of the  
15  $^1\text{H}^{15}\text{N}$  TROSY spectra of substrate-free  $\beta$ PGM<sub>D10N</sub> and  $\beta$ PGM<sub>WT</sub> indicated that  $\beta$ PGM<sub>D10N</sub>  
16 adopts a native conformation following refolding (Figure S3A).  
17  
18  
19  
20  
21  
22  
23  
24  
25  
26  
27  
28  
29  
30  
31  
32  
33  
34  
35  
36  
37  
38  
39  
40  
41  
42  
43  
44  
45  
46  
47  
48  
49  
50  
51  
52  
53  
54  
55  
56  
57  
58  
59  
60



1  
2  
3 **Figure 2.** NMR spectra and reaction kinetics of  $\beta$ PGM<sub>D10N</sub>. (A)  $^{31}\text{P}$  spectrum of  $\beta$ PGM<sub>D10N</sub>  
4 immediately following purification showing four  $^{31}\text{P}$  peaks (5.17, 5.08, 2.01 and 1.30 ppm)  
5  
6  
7  
8  
9  
10 (ratio 6:5). Resonances at ~5 ppm and 1–2 ppm correspond to 6-phosphate and 1-phosphate  
11 groups of  $\beta$ G16BP, respectively. (B) Overlay of a section of  $^1\text{H}^{15}\text{N}$  TROSY spectra for a range  
12 of  $\beta$ PGM<sub>D10N</sub> complexes: (black) substrate-free  $\beta$ PGM<sub>D10N</sub>; (pink)  $\beta$ PGM<sub>D10N</sub>:BeF<sub>3</sub> complex;  
13  
14 of  $\beta$ PGM<sub>D10N</sub> complexes: (black) substrate-free  $\beta$ PGM<sub>D10N</sub>; (pink)  $\beta$ PGM<sub>D10N</sub>:BeF<sub>3</sub> complex;  
15  
16 (red)  $\beta$ PGM<sub>D10N</sub><sup>P</sup> –  $^1\text{H}^{15}\text{N}$  BEST-TROSY spectrum started 6 min after addition of 20 mM AcP to  
17  
18 substrate-free  $\beta$ PGM<sub>D10N</sub>; (gray) substrate-free  $\beta$ PGM<sub>D10N</sub> –  $^1\text{H}^{15}\text{N}$  BEST-TROSY spectrum  
19  
20 started after a further 92 min by which time AcP has been depleted and  $\beta$ PGM<sub>D10N</sub><sup>P</sup> has reverted  
21  
22 to substrate-free  $\beta$ PGM<sub>D10N</sub> (the small shift in peak positions is caused by an increase in  
23  
24 inorganic phosphate concentration); (magenta)  $\beta$ PGM<sub>D10N</sub><sup>P</sup> as major species –  $^1\text{H}^{15}\text{N}$  BEST-  
25  
26 TROSY spectrum started 6 min after addition of 10 mM G6P and 20 mM AcP to substrate-free  
27  
28  $\beta$ PGM<sub>D10N</sub>; (blue)  $\beta$ PGM<sub>D10N</sub>: $\beta$ G16BP complexes –  $^1\text{H}^{15}\text{N}$  BEST-TROSY spectrum started after  
29  
30 a further 145 min by which time AcP has been depleted and the  $\beta$ PGM<sub>D10N</sub>: $\beta$ G16BP complexes  
31  
32 dominate in solution. The arrows indicate progression for the assigned residues from (black)  
33  
34 substrate-free  $\beta$ PGM<sub>D10N</sub> to (magenta)  $\beta$ PGM<sub>D10N</sub><sup>P</sup> to (blue) the  $\beta$ PGM<sub>D10N</sub>: $\beta$ G16BP complexes.  
35  
36  
37 (C and D) Michaelis-Menten plots showing the dependence of the reaction velocity ( $v$ ) for 5 nM  
38  
39  $\beta$ PGM<sub>WT</sub> (black circles; n=3) and 500 nM substrate-free  $\beta$ PGM<sub>D10N</sub> (red circles; n=3) on the  
40  
41 initial  $\beta$ G1P concentration, monitored using a glucose 6-phosphate dehydrogenase coupled  
42  
43 assay. Data were fitted to the standard Michaelis-Menten equation to derive  $k_{\text{cat}}$  and  $K_{\text{m}}$  values  
44  
45 and the line of best fit is shown for  $\beta$ PGM<sub>WT</sub> (gray) and substrate-free  $\beta$ PGM<sub>D10N</sub> (pink).  
46  
47  
48  
49  
50  
51  
52  
53  
54  
55  
56  
57  
58  
59  
60



1  
2  
3 **Substrate-free  $\beta$ PGMD10N readily forms a transient phospho-enzyme.**  $\beta$ PGM<sub>WT</sub> can be  
4 phosphorylated to generate  $\beta$ PGM<sub>WT</sub><sup>P</sup> by a number of priming agents, including not only  
5  $\beta$ G16BP (Figure 1A) but also  $\alpha$ G16BP, G6P, and acetyl phosphate (AcP) (17, 30). In order to  
6 establish whether  $\beta$ PGMD10N could be similarly phosphorylated, incubation of 1 mM substrate-  
7 free  $\beta$ PGMD10N with 20 mM AcP was followed using a time course of <sup>1</sup>H<sup>15</sup>N BEST-TROSY  
8 spectra (32, 33) with 6 min time resolution (Figure 2B). The initial spectra overlaid closely with  
9  
10  
11  
12  
13  
14  
15  
16  
17  
18 a <sup>1</sup>H<sup>15</sup>N TROSY spectrum of the  $\beta$ PGMD10N:BeF<sub>3</sub> complex, which is an analogue of  $\beta$ PGMD10N  
19 prepared using conditions described previously for the  $\beta$ PGM<sub>WT</sub>:BeF<sub>3</sub> complex (Figure S3B)  
20  
21  
22 (23). This established that  $\beta$ PGMD10N<sup>P</sup> is generated during the 6 min dead-time of the time  
23 course. After 98 min, the <sup>1</sup>H<sup>15</sup>N BEST-TROSY spectrum had reverted entirely to that of  
24 substrate-free  $\beta$ PGMD10N. Monitoring the same reaction using <sup>31</sup>P NMR spectra, the hydrolysis  
25 rate constant for  $\beta$ PGMD10N<sup>P</sup> was determined to be  $0.020 \pm 0.002 \text{ s}^{-1}$  (Figure S3C). The  
26 equivalent rate constant for  $\beta$ PGM<sub>WT</sub><sup>P</sup> under the same conditions is only 3 fold greater ( $0.060 \pm$   
27  $0.006 \text{ s}^{-1}$ ), indicating that the proposed general acid-base (D10) has little involvement in the  
28 attack of  $\beta$ PGM<sup>P</sup> by water. Attempts to crystallize the meta-stable species  $\beta$ PGMD10N<sup>P</sup> were  
29 unsuccessful. However, the  $\beta$ PGMD10N:BeF<sub>3</sub> complex was crystallized and the structure was  
30 determined to 1.3 Å resolution (PDB 5OJZ; Figure 3 A and G, Figure S4A and Table S1). The  
31 cap and core domains were in a predominantly open conformation, as in the  $\beta$ PGM<sub>WT</sub>:BeF<sub>3</sub>  
32 complex (PDB 2WFA (23); non-H atom RMSD = 1.06 Å), and the sidechain of residue N10 was  
33 in the *out* position (Figure 1B), thereby not positioned to contribute to the nucleophilic attack of  
34  $\beta$ PGMD10N<sup>P</sup> by water. The close similarity of <sup>1</sup>H<sup>15</sup>N TROSY spectra between  $\beta$ PGM<sub>WT</sub>:BeF<sub>3</sub>,  
35  
36  
37  
38  
39  
40  
41  
42  
43  
44  
45  
46  
47  
48  
49  
50  
51  
52  
53  
54  
55  
56  
57  
58  
59  
60

$\beta\text{PGM}_{\text{D10N}}:\text{BeF}_3$  and  $\beta\text{PGM}_{\text{D10N}}^{\text{P}}$  indicates that these structural features are common to all three species in solution.

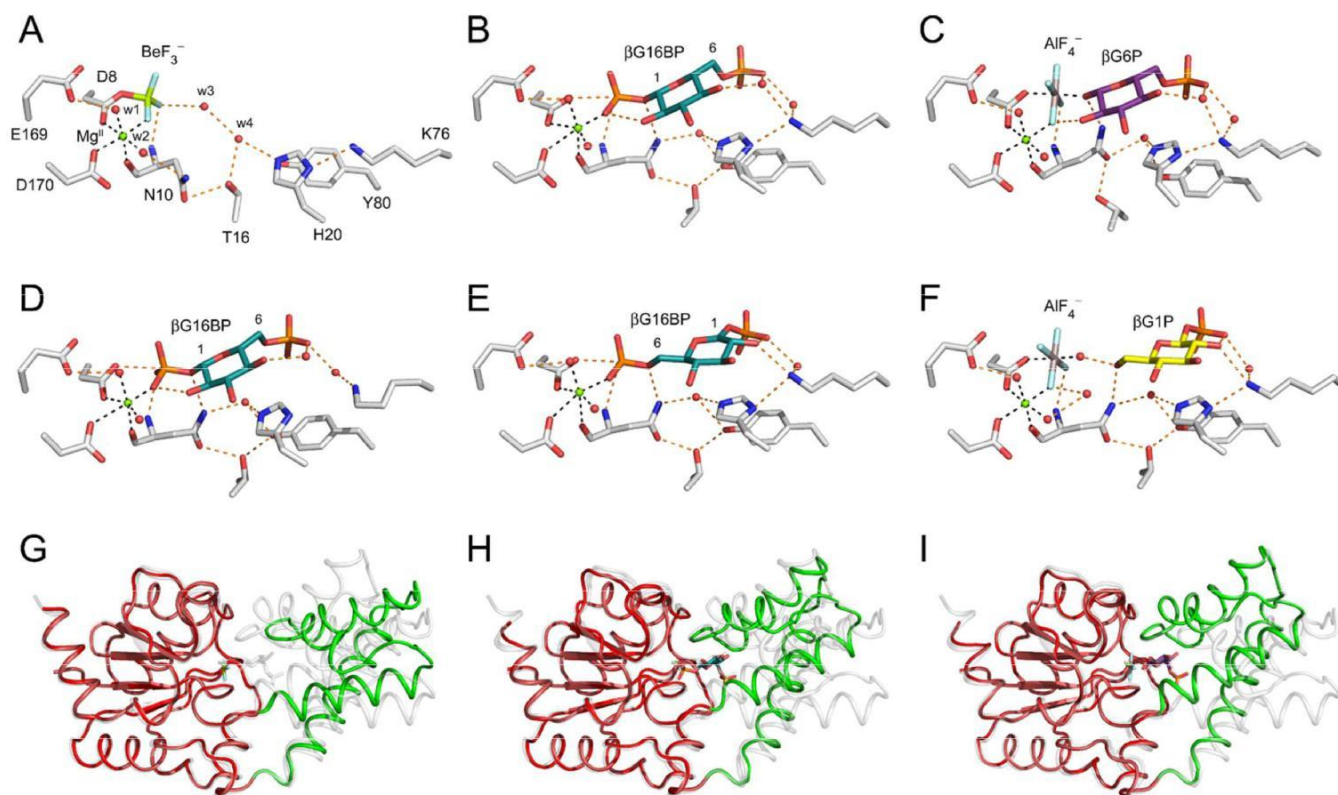


**Figure 3.** Overviews of the active sites and the extent of domain closure in the  $\beta\text{PGM}_{\text{D10N}}$  complexes. The active sites of (A)  $\beta\text{PGM}_{\text{D10N}}:\text{BeF}_3$  complex (PDB 5OJZ), (B)  $\beta\text{PGM}_{\text{D10N}}:\text{P1G6P}$  complex (PDB 5OK1), (C)  $\beta\text{PGM}_{\text{D10N}}:\text{AlF}_4:\text{G6P}$  complex (PDB 5OK2), (D) co-purified  $\beta\text{PGM}_{\text{D10N}}:\text{P1G6P}$  complex (PDB 5O6P), (E)  $\beta\text{PGM}_{\text{D10N}}:\text{P6G1P}$  complex (PDB 5OK0) and (F)  $\beta\text{PGM}_{\text{D10N}}:\text{AlF}_4:\text{H}_2\text{O}:\beta\text{G1P}$  complex (PDB 5O6R). Selected active site residues and ligands are shown as sticks in standard CPK colors, with beryllium (light green), fluorine (light blue), aluminum (dark gray),  $\beta\text{G16BP}$  (teal carbon atoms; with C1 and C6 labeled for clarity), G6P (purple carbon atoms) and  $\beta\text{G1P}$  (gold carbon atoms). Structural waters (red) and

1  
2  
3 the catalytic  $\text{Mg}^{\text{II}}$  ion (green) are drawn as spheres. Orange dashes indicate hydrogen bonds and  
4  
5 black dashes show metal ion coordination. The extent of domain closure is shown in (G)  
6  
7  $\beta\text{PGM}_{\text{D10N}}:\text{BeF}_3$  complex (PDB 5OJZ), (H)  $\beta\text{PGM}_{\text{D10N}}:\text{P1G6P}$  complex (PDB 5OK1) and (I)  
8  
9  $\beta\text{PGM}_{\text{D10N}}:\text{AlF}_4:\text{G6P}$  complex (PDB 5OK2). The protein backbone of  $\beta\text{PGM}_{\text{D10N}}$  is depicted as  
10  
11 a ribbon, with the core (red) and the cap (green) domains indicated and the ligands shown as sticks  
12  
13 and spheres (colored as above). The pale gray ribbons indicate the open  $\beta\text{PGM}_{\text{WT}}$  structure (PDB  
14  
15 2WHE (20)) and the fully closed  $\beta\text{PGM}_{\text{WT}}:\text{MgF}_3:\text{G6P}$  TSA complex (PDB 2WF5 (20))  
16  
17 superposed on the core domains to show the extent of domain closure in the  $\beta\text{PGM}_{\text{D10N}}$   
18  
19  
20  
21  
22  
23  
24  
25  
26  
27  
28  
29  
30  
31  
32  
33  
34  
35  
36  
37  
38  
39  
40  
41  
42  
43  
44  
45  
46  
47  
48  
49  
50  
51  
52  
53  
54  
55  
56  
57  
58  
59  
60

**The substrate-free  $\beta\text{PGM}_{\text{D10N}}$  preparation has mutase activity.** In addition to substrate-free  $\beta\text{PGM}_{\text{D10N}}$  having similar levels of phosphatase activity to  $\beta\text{PGM}_{\text{WT}}$ , the substrate-free  $\beta\text{PGM}_{\text{D10N}}$  preparation was also found to have mutase activity. The standard glucose 6-phosphate dehydrogenase coupled assay (8, 17, 18) was used to monitor conversion of  $\beta\text{G1P}$  to G6P using AcP as the priming agent. The kinetic profile displayed the characteristic lag phase for  $\beta\text{PGM}$  (Figure S3 I and J) (30), and a simple steady-state Michaelis-Menten analysis of the linear portion (Figure 2D), yielded values for  $k_{\text{cat}}$  of  $0.15 \pm 0.01 \text{ s}^{-1}$  and  $K_{\text{m}}$  of  $150 \pm 12 \mu\text{M}$ . Measurements under the same conditions for  $\beta\text{PGM}_{\text{WT}}$  (Figure 2C), yielded values of  $24.5 \pm 0.7 \text{ s}^{-1}$  and  $92 \pm 6 \mu\text{M}$ , respectively; minor levels of inhibition by the priming agent (17, 30) is a likely source of the slightly different values determined here compared with some reported previously for  $\beta\text{PGM}_{\text{WT}}$  (8, 30). Contaminating *E. coli*  $\beta\text{PGM}_{\text{WT}}$  is unlikely to be the source of mutase activity in the substrate-free  $\beta\text{PGM}_{\text{D10N}}$  preparation as there is no equilibration of  $\beta\text{G1P}$

1  
2  
3 with G6P over a similar timeframe by  $\beta$ PGM<sub>D8N</sub> (Figure S3D), which has identical  
4  
5 chromatography retention characteristics to  $\beta$ PGM<sub>D10N</sub>. To investigate whether the activity of the  
6  
7 substrate-free  $\beta$ PGM<sub>D10N</sub> preparation was the result of recovery by acetate (derived from AcP  
8  
9 hydrolysis) substituting for the general acid-base, the equilibration of  $\beta$ G1P with G6P was  
10  
11 primed with  $\beta$ G16BP rather than AcP (Figure S3E). Mutase activity was again observed (with a  
12  
13 slightly larger rate constant,  $k_{\text{cat}} = 0.6 \text{ s}^{-1}$ , as there is no inhibition when  $\beta$ G16BP is used as the  
14  
15 priming agent) and thus acetate was not playing a significant role in recovery of activity. In  
16  
17 contrast, it has not been possible to eliminate low levels ( $\sim 0.6\%$ ) of contaminating *L. lactis*  
18  
19  $\beta$ PGM<sub>WT</sub> as the source of mutase activity because the measured  $K_m$  values, and degree of  
20  
21 inhibition by inorganic phosphate (Figure S3F), and by fluoride (Figure S3G) are not sufficiently  
22  
23 different between the substrate-free  $\beta$ PGM<sub>D10N</sub> preparation and  $\beta$ PGM<sub>WT</sub>. Low levels of  
24  
25  $\beta$ PGM<sub>WT</sub> can potentially be formed by translational mis-incorporation or by deamidation of  
26  
27  $\beta$ PGM<sub>D10N</sub> during refolding, where the N10-G11 sequence will have elevated susceptibility (51).  
28  
29 However, it is difficult to rationalize the dominant effect arising either from translational mis-  
30  
31 incorporation, when an increase in mutase activity is observed following  $\beta$ G16BP removal ( $k_{\text{cat}} =$   
32  
33  $0.002 \text{ s}^{-1}$  for co-purified  $\beta$ PGM<sub>D10N</sub> vs  $k_{\text{cat}} = 0.2 \text{ s}^{-1}$  for the substrate-free  $\beta$ PGM<sub>D10N</sub>  
34  
35 preparation), or from deamidation, when only a 2-fold increase in activity is observed following  
36  
37 2 h vs 48 h incubation with 4 M guanidine hydrochloride prior to refolding (Figure S3 K and L).  
38  
39  
40  
41  
42  
43  
44  
45  
46  
47

48 **Substrate-free  $\beta$ PGM<sub>D10N</sub> slowly reforms stable  $\beta$ G16BP complexes.** In order to establish  
49  
50 that the substrate-free  $\beta$ PGM<sub>D10N</sub> preparation was capable of reconstituting the  
51  
52  $\beta$ PGM<sub>D10N</sub>: $\beta$ G16BP complexes *in situ*, the equilibration of 10 mM  $\beta$ G1P with G6P (and *vice*  
53  
54  
55  
56  
57  
58  
59  
60

1  
2  
3 *versa*) by 1 mM substrate-free  $\beta$ PGMD10N in the presence of 20 mM AcP was monitored using a  
4  
5 time course of  $^1\text{H}^{15}\text{N}$  BEST-TROSY spectra with 6 min time resolution (Figure 2B). At this  
6  
7 concentration of substrate-free  $\beta$ PGMD10N,  $\beta$ G1P and G6P were fully equilibrated (*via*  $\beta$ G16BP,  
8  
9 Figure 1A) in the 6 min dead-time of the time course, and the initial enzyme species observed  
10  
11 was  $\beta$ PGMD10N<sup>P</sup>.  $\beta$ PGMD10N<sup>P</sup> was slowly replaced ( $k_{\text{obs}} = 5 \times 10^{-4} \text{ s}^{-1}$ ) by two conformationally  
12  
13 distinct species (Figure S5), that reproduce the  $^{31}\text{P}$  NMR spectrum of the co-purified  
14  
15  $\beta$ PGMD10N: $\beta$ G16BP complexes (Figure 2A). When 20 mM AcP and 10 mM  $\beta$ G1P were added to  
16  
17 the reconstituted  $\beta$ PGMD10N: $\beta$ G16BP complex preparation, the rate constant of equilibration was  
18  
19 within error of that of the original substrate-free  $\beta$ PGMD10N preparation (Figure S3H).  
20  
21  
22  
23  
24  
25  
26

### **The nucleophile in the $\beta$ PGMD10N:P1G6P complex is aligned for attack.**

The

27  
28  $\beta$ PGMD10N: $\beta$ G16BP complexes were explored using X-ray crystallography to compare their  
29  
30 structures with those of metal fluoride analogue complexes (19, 20, 23). A reconstituted  
31  
32  $\beta$ PGMD10N: $\beta$ G16BP complex was crystallized and the structure was determined to 1.9 Å  
33  
34 resolution (PDB 5OK1; Figure 3 B and H, Figure S4B and Table S1). In this structure,  $\beta$ G16BP  
35  
36 is bound in a single orientation, with the 1-phosphate in the *proximal* site and the 6-phosphate in  
37  
38 the *distal* site, and is hence termed the  $\beta$ PGMD10N:P1G6P complex. This structure mimics the  
39  
40 active site conformation immediately preceding phosphoryl transfer from  $\beta$ G16BP to  $\beta$ PGM in  
41  
42 Step 2 (Figure 1A). This conformation requires a protonated general acid-base and its surrogate,  
43  
44 N10, forms a hydrogen bond through its sidechain amide group to the bridging oxygen of the 1-  
45  
46 phosphate of  $\beta$ G16BP. The 1-phosphorus atom is positioned in-line for attack by D8 atom O $\delta$ 1  
47  
48 (O - P - O angle =  $170^\circ$ ) with a donor-acceptor oxygen atom separation of 4.6 Å and a  
49  
50 nucleophile-phosphorus distance of 3.0 Å, which is inside the sum of the van der Waals radii for  
51  
52  
53  
54  
55  
56  
57  
58  
59  
60

1  
2  
3 these two atoms (3.3 Å) (Figure 3B) (52). The donor-acceptor oxygen atom separation is larger  
4  
5 than is observed in TSA complexes containing  $\text{AlF}_4^-$  (3.9 Å; PDB 2WF6) and  $\text{MgF}_3^-$  (4.3 Å;  
6  
7 PDB 2WF5 (20)) and in some DFT models of the TS for this chemical step in  $\beta\text{PGM}_{\text{WT}}$ , (4.2 Å  
8  
9 (11); 4.4 Å (12)). A co-purified  $\beta\text{PGM}_{\text{D10N}}:\beta\text{G16BP}$  complex was also crystallized and the  
10  
11 structure was determined to 2.2 Å resolution (PDB 5O6P; Figure 3D, Figure S4C and Table S1). In  
12  
13 this structure,  $\beta\text{G16BP}$  is bound in the same orientation as that present in the reconstituted  
14  
15  $\beta\text{PGM}_{\text{D10N}}:\text{P1G6P}$  complex and the two complexes overlay closely with a non-H atom RMSD =  
16  
17  
18 0.43 Å (Figure S6 and Table S2). The active site arrangement present in both  $\beta\text{PGM}_{\text{D10N}}:\text{P1G6P}$   
19  
20  
21 complexes conforms to the definition of an aligned NAC (23, 26), where atomic distances and  
22  
23 geometries lie close to those of TS models (25). Given the close similarity between the complexes,  
24  
25 the structure of the reconstituted  $\beta\text{PGM}_{\text{D10N}}:\beta\text{G16BP}$  complex will be used in the  
26  
27  
28 comparisons described below.  
29  
30  
31

32  
33  
34 **The  $\beta\text{PGM}_{\text{D10N}}:\text{P1G6P}$  complex is not fully closed.** In contrast to all deposited metal  
35  
36 fluoride analogue  $\beta\text{PGM}$  structures, the alignment of the nucleophile in the  $\beta\text{PGM}_{\text{D10N}}:\text{P1G6P}$   
37  
38 complex is satisfied without full closure of the enzyme (Figure 3 B and H and Table S2).  
39  
40 Compared to the  $\beta\text{PGM}_{\text{WT}}:\text{MgF}_3:\text{G6P}$  TSA complex (PDB 2WF5 (20)), the relative orientation  
41  
42 of the cap and core domains undergoes a rotation of  $13^\circ$ , and there are significant changes in the  
43  
44 hydrogen bonding network within the vicinity of the general acid-base residue. N10 donates a  
45  
46 hydrogen bond to  $\beta\text{G16BP}$  (through atom N $\delta$ 2), while simultaneously accepting a hydrogen  
47  
48 bond (through atom O $\delta$ 1) from the backbone amide NH and the sidechain OH groups of T16.  
49  
50 Crucially, residue T16 dictates the relative degree of closure of the cap and core domains (8, 23),  
51  
52 and in the  $\beta\text{PGM}_{\text{D10N}}:\text{P1G6P}$  complex the conformation of T16 is near the midpoint of the  
53  
54  
55  
56  
57  
58  
59  
60

1  
2  
3 transition between the substrate-free  $\beta$ PGM<sub>WT</sub> and the  $\beta$ PGM<sub>WT</sub>:MgF<sub>3</sub>:G6P TSA structures. The  
4  
5 inference is that van der Waals contact between the attacking nucleophile and the 1-phosphorus  
6  
7 atom of  $\beta$ G16BP in the  $\beta$ PGM<sub>D10N</sub>:P1G6P complex, resists a donor-acceptor oxygen atom  
8  
9 separation of less than 4.6 Å, the effect of which propagates through the structure to prevent the  
10  
11 TS hydrogen bonding organization and full domain closure from being established (11–13, 20).  
12  
13 Moreover, asymmetrical electron density for the catalytic Mg<sup>II</sup> ion in the  $\beta$ PGM<sub>D10N</sub>:P1G6P  
14  
15 complex shows clear evidence of a deviation from optimal octahedral coordination geometry  
16  
17 (Figure S7A), with elongation of distances and distortion of angles, that is not observed in metal  
18  
19 fluoride-based ground and transition state analogue complexes of  $\beta$ PGM. This result implies that  
20  
21 a competition exists in Mg<sup>II</sup> ion coordination between the oxygen atom of the 1-phosphate group  
22  
23 of  $\beta$ G16BP (O – Mg<sup>II</sup> = 2.0 Å) and the carboxylate oxyanion of residue D170 (O – Mg<sup>II</sup> = 2.6  
24  
25 Å). The equilibrium position of the Mg<sup>II</sup> ion lies towards coordination by the phosphate oxygen  
26  
27 atom, which is expected to have a higher anionic charge density, with subsequent compromising  
28  
29 of coordination by enzymatic oxygen and oxyanion ligands. Together, these observations  
30  
31 illustrate the interdependency between donor and acceptor atom separation, optimal hydrogen  
32  
33 bond organization, optimal catalytic Mg<sup>II</sup> ion coordination, and full domain closure to achieve  
34  
35 TS architecture.  
36  
37  
38  
39  
40  
41  
42  
43  
44

45 **The  $\beta$ PGM<sub>D10N</sub>:AlF<sub>4</sub>:G6P TSA complex is fully closed.** In order to establish that the  
46  
47 antagonism of full closure in the  $\beta$ PGM<sub>D10N</sub>:P1G6P complex was not simply an artefact of the  
48  
49 aspartate to asparagine substitution, the  $\beta$ PGM<sub>D10N</sub>:AlF<sub>4</sub>:G6P TSA complex was crystallized and  
50  
51 the structure was determined to 1.1 Å resolution (PDB 5OK2; Figure 3 C and I, Figure S4D and  
52  
53 Table S1). This complex superimposes very closely with the  $\beta$ PGM<sub>WT</sub>:AlF<sub>4</sub>:G6P TSA complex  
54  
55  
56  
57  
58  
59  
60

1  
2  
3 (PDB 2WF6; non-H atom RMSD = 0.13 Å) and it binds G6P with the 6-phosphate in the *distal*  
4  
5 site and the square planar  $\text{AlF}_4^-$  moiety mimicking the transferring phosphoryl group in the  
6  
7 *proximal* site between D8 (atom O $\delta$ 1) and the 1-OH group of G6P (53). The donor-acceptor  
8  
9 distance and angle of alignment are identical to those in the  $\beta\text{PGM}_{\text{WT}}:\text{AlF}_4:\text{G6P}$  TSA complex  
10  
11 (3.8 Å and 173°, respectively). However, a comparison of the hydrogen bonding arrangements  
12  
13 between D10/N10 and the 1-oxygen of G6P in the  $\beta\text{PGM}_{\text{WT}}:\text{AlF}_4:\text{G6P}$  TSA and the  
14  
15  $\beta\text{PGM}_{\text{D10N}}:\text{AlF}_4:\text{G6P}$  TSA complexes reveals a difference in the identity of the proton donor and  
16  
17 proton acceptor. Whereas in the  $\beta\text{PGM}_{\text{WT}}:\text{AlF}_4:\text{G6P}$  TSA complex, the transferring proton is  
18  
19 bonded to the 1-OH group of G6P and is coordinated by the anionic carboxylate group of the  
20  
21 general acid-base, the analogous hydrogen bond in the  $\beta\text{PGM}_{\text{D10N}}:\text{AlF}_4:\text{G6P}$  TSA complex has  
22  
23 the sidechain  $\text{NH}_2$  group of N10 coordinated by what is likely to be the deprotonated 1-oxygen  
24  
25 of G6P. Owing to the ability of the active site to accommodate the D10 to N10 substitution, the  
26  
27  $\beta\text{PGM}_{\text{D10N}}$  variant is capable of full domain closure with concomitant formation of TS geometry.  
28  
29  
30  
31  
32  
33  
34  
35

36 **The  $\beta\text{PGM}_{\text{D10N}}:\text{P6G1P}$  complex closely resembles the  $\beta\text{PGM}_{\text{D10N}}:\text{P1G6P}$  complex.** While  
37  
38 crystals harvested after 12 weeks consisted exclusively of the  $\beta\text{PGM}_{\text{D10N}}:\text{P1G6P}$  complex, a  
39  
40 crystal with the same morphology harvested from the same drop after only 1 week yielded a 2.2  
41  
42 Å resolution structure of a different complex. While the resolution of the structure was limited,  
43  
44 the electron density clearly showed that the structure contained  $\beta\text{G16BP}$  bound in the alternate  
45  
46 orientation, with the 6-phosphate in the *proximal* site and the 1-phosphate in the *distal* site, and is  
47  
48 hence termed the  $\beta\text{PGM}_{\text{D10N}}:\text{P6G1P}$  complex (PDB 5OK0; Figure 3E, Figure S4E and Table  
49  
50 S1). Overall, the orientation of  $\beta\text{G16BP}$  does not have a strong influence on the degree of  
51  
52 domain closure in the  $\beta\text{PGM}_{\text{D10N}}:\beta\text{G16BP}$  complexes (non-H atom RMSD = 0.34 Å). The  
53  
54  
55  
56  
57  
58  
59  
60



1  
2  
3 relative orientation of the cap and core domains compared to the  $\beta$ PGM<sub>D10N</sub>:AlF<sub>4</sub>:G6P TSA  
4  
5 complex have rotations of 13° ( $\beta$ PGM<sub>D10N</sub>:P1G6P) and 14° ( $\beta$ PGM<sub>D10N</sub>:P6G1P) (Table S2). The  
6  
7  $\beta$ PGM<sub>D10N</sub>:P6G1P complex can again be defined as an aligned NAC (O – P – O angle = 176°, a  
8  
9 donor-acceptor oxygen atom separation of 4.7 Å and a nucleophile-phosphorus distance of 3.1 Å)  
10  
11 and the hydrogen bonding of residue N10 is analogous to that present in the  $\beta$ PGM<sub>D10N</sub>:P1G6P  
12  
13 complex. There is also a direct hydrogen bond present between the sidechain OH group of S52 and  
14  
15 the 3-OH group of  $\beta$ G16BP in the  $\beta$ PGM<sub>D10N</sub>:P6G1P complex, whereas in  
16  
17 the  $\beta$ PGM<sub>D10N</sub>:P1G6P complex, hydrogen bonding between  $\beta$ G16BP and the protein is mediated  
18  
19 by two water molecules (Figure S8), as observed previously in TSA complexes involving G6P  
20  
21 and  $\beta$ -glucose 1-phosphonates (19). Hence, alignment of the  $\beta$ G16BP intermediate is achieved in  
22  
23 both  $\beta$ PGM<sub>D10N</sub>: $\beta$ G16BP complexes without full closure of the enzyme.  
24  
25  
26  
27  
28  
29  
30  
31

32 **The  $\beta$ PGM<sub>D10N</sub>:AlF<sub>4</sub>:H<sub>2</sub>O: $\beta$ G1P complex is partially open.** The structure of the  
33  
34  $\beta$ PGM<sub>D10N</sub>:AlF<sub>4</sub>: $\beta$ G1P complex was investigated to ascertain if it behaved analogously to the  
35  
36  $\beta$ PGM<sub>D10N</sub>:AlF<sub>4</sub>:G6P TSA complex, thus providing a direct comparator for the  
37  
38  $\beta$ PGM<sub>D10N</sub>:P6G1P complex. The crystal structure of the  $\beta$ PGM<sub>D10N</sub>:AlF<sub>4</sub>: $\beta$ G1P complex was  
39  
40 determined to 1.4 Å resolution (PDB 5O6R; Figure 3F, Figure S4F and Table S1). Surprisingly,  
41  
42 the structure did not resemble that of the fully closed  $\beta$ PGM<sub>WT</sub>:AlF<sub>4</sub>:G6P TSA complex (PDB  
43  
44 2WF6), but instead the protein atoms superimposed almost exactly with the partially open  
45  
46  $\beta$ PGM<sub>D10N</sub>:P6G1P complex (non-H atom RMSD = 0.33 Å). Uniquely in  $\beta$ PGM structures,  
47  
48 electron density consistent with a water molecule occupying an axial ligand position of the AlF<sub>4</sub><sup>-</sup>  
49  
50 moiety (instead of the 6-oxygen of  $\beta$ G1P) was present, with D8 still occupying the other axial  
51  
52  
53  
54  
55  
56  
57  
58  
59  
60

1  
2  
3 position, and this structure is hence termed a  $\beta\text{PGM}_{\text{D10N}}:\text{AlF}_4:\text{H}_2\text{O}:\beta\text{G1P}$  complex. The water  
4  
5 molecule satisfies the demands of the  $\text{AlF}_4^-$  moiety for octahedral coordination while allowing  
6  
7 the cap domain and hydrogen bonding pattern between N10, T16 and D15 to adopt that of the  
8  
9  $\beta\text{PGM}_{\text{D10N}}:\text{P6G1P}$  complex. The sidechain  $\text{NH}_2$  group of N10 remains hydrogen bonded to the  
10  
11 6-OH group of  $\beta\text{G1P}$  rather than switching to the water molecule, despite the 6-OH group of  
12  
13  $\beta\text{G1P}$  being located further from D8 ( $6\text{-OH} - \text{O}\delta 1 = 5.7 \text{ \AA}$ ), compared with the 6-oxygen of  
14  
15  $\beta\text{G16BP}$  in the  $\beta\text{PGM}_{\text{D10N}}:\text{P6G1P}$  structure ( $6\text{-O} - \text{O}\delta 1 = 4.6 \text{ \AA}$ ). This structure implies that  
16  
17 there is greater resistance to the formation of the fully closed  $\beta\text{PGM}_{\text{D10N}}:\text{AlF}_4^-$  TSA complex  
18  
19 with  $\beta\text{G1P}$  than with G6P. In contrast to the apparent deprotonation of the 1-oxygen of G6P in  
20  
21 the  $\beta\text{PGM}_{\text{D10N}}:\text{AlF}_4:\text{G6P}$  TSA complex, deprotonation of the 6-OH group of  $\beta\text{G1P}$  appears not  
22  
23 to be the preferred arrangement in the  $\beta\text{PGM}_{\text{D10N}}:\text{AlF}_4:\beta\text{G1P}$  complex, correlating with the  $\sim 3$   
24  
25 unit difference in solution  $\text{p}K_{\text{a}}$  values for the two hydroxyl groups (54).  
26  
27  
28  
29  
30  
31  
32  
33  
34

35 **The  $\beta\text{PGM}_{\text{D10N}}:\text{P1G6P}$  complex dominates in solution.** The crystal structures of the  
36  
37  $\beta\text{PGM}_{\text{D10N}}:\beta\text{G16BP}$  complexes with the intermediate bound in the two orientations presents a  
38  
39 rationale for the non-equivalent complexes observed in solution using  $^{31}\text{P}$  and  $^1\text{H}^{15}\text{N}$  TROSY  
40  
41 NMR approaches (Figure 2A and Figure S5). In the  $\beta\text{PGM}_{\text{D10N}}:\text{P1G6P}$  complex (Figure 3B),  
42  
43 there is close proximity between H4 of  $\beta\text{G16BP}$  and the imidazole group of residue H20, which  
44  
45 should result in a marked upfield chemical shift change of the H4 resonance through aromatic  
46  
47 ring current effects. In the  $\beta\text{PGM}_{\text{D10N}}:\text{P6G1P}$  complex (Figure 3E), this chemical shift change  
48  
49 should instead be experienced by the H3 resonance because of the change in orientation of the  
50  
51  $\beta\text{G16BP}$  ligand. To investigate the two  $\beta\text{PGM}_{\text{D10N}}:\beta\text{G16BP}$  complexes in solution,  $^1\text{H}^{13}\text{C}$  HSQC  
52  
53  
54  
55  
56  
57  
58  
59  
60

1  
2  
3 and CCH-TOCSY spectra were acquired using 1:1  $\beta$ PGM<sub>D10N</sub> and 100% U-<sup>13</sup>C- $\beta$ G16BP (Figure  
4 S2C). In both  $\beta$ PGM<sub>D10N</sub>: $\beta$ G16BP complexes only the H4 resonance of  $\beta$ G16BP is shifted  
5  
6 markedly upfield on binding ( $\Delta\delta = 1.05$  and  $1.18$  ppm), while the H3 resonance of  $\beta$ G16BP is  
7  
8 shifted slightly downfield ( $\Delta\delta = 0.08$  and  $0.14$  ppm). Together, these results indicate that the  
9  
10 bound orientation of  $\beta$ G16BP is the same in the two solution forms, thus identifying both as  
11  
12  $\beta$ PGM<sub>D10N</sub>:P1G6P complexes. The dominance of  $\beta$ PGM<sub>D10N</sub>:P1G6P over  $\beta$ PGM<sub>D10N</sub>:P6G1P  
13  
14 complexes in solution mirrors the relative dissociation constants for G6P ( $9 \mu\text{M}$ ) and  $\beta$ G1P ( $46$   
15  
16  $\mu\text{M}$ ) in the  $\beta$ PGM<sub>WT</sub>:AlF<sub>4</sub><sup>-</sup> TSA complexes (19).  
17  
18  
19  
20  
21  
22  
23  
24

25 **The  $\beta$ PGM<sub>D10N</sub>:P1G6P complex has weak Mg<sup>II</sup> affinity.** The source of the difference  
26  
27 between the two solution  $\beta$ PGM<sub>D10N</sub>:P1G6P complexes was investigated using NMR backbone  
28  
29 resonance assignment. All 210 of the non-proline residues were assigned, of which 115 showed  
30  
31 more than one spin system. No significant structural differences were identified upon calculation  
32  
33 of dihedral angles using TALOS-N (55) (Figure S5 E and F). Residues with the largest chemical  
34  
35 shift differences between the two complexes were principally located within the active site  
36  
37 (Figure S5G). For <sup>15</sup>N, these comprise L9 ( $-2.29$  ppm), V47 ( $-2.15$  ppm), V141 ( $-2.78$  ppm)  
38  
39 and D170 ( $-2.16$  ppm), for <sup>13</sup>C', N10 ( $-2.69$  ppm) and D170 ( $-1.74$  ppm), for <sup>13</sup>C $\alpha$ , D8 ( $0.81$   
40  
41 ppm), N10 ( $-0.86$  ppm) and S144 ( $-0.90$  ppm), and for <sup>13</sup>C $\beta$ , K45 ( $-0.80$  ppm) and S171 ( $-0.93$   
42  
43 ppm) (Figure S5 A and B). Residues N10 and D170 are involved with the ligation of the catalytic  
44  
45 Mg<sup>II</sup> ion, suggesting that changes in this coordination may be responsible for the chemical shift  
46  
47 differences observed. To investigate, an Mg<sup>II</sup>-free form of the  $\beta$ PGM<sub>D10N</sub>:P1G6P complex was  
48  
49 prepared and the <sup>1</sup>H<sup>15</sup>N-TROSY spectrum corresponded to one of the assigned  
50  
51  $\beta$ PGM<sub>D10N</sub>:P1G6P complexes, while addition of Mg<sup>II</sup> resulted in the other. Overall, the backbone  
52  
53  
54  
55  
56  
57  
58  
59  
60

1  
2  
3 chemical shift differences between the  $\text{Mg}^{\text{II}}$ -bound and  $\text{Mg}^{\text{II}}$ -free  $\beta\text{PGM}_{\text{D10N}}:\text{P1G6P}$  complexes  
4 are reminiscent of those between the  $\beta\text{PGM}_{\text{WT}}:\text{MgF}_3:\text{G6P}$  TSA complex (BMRB 7234 (20)) and  
5 the  $\text{Mg}^{\text{II}}$ -bound  $\beta\text{PGM}_{\text{D10N}}:\text{P1G6P}$  complex in terms of the residues involved, but are smaller in  
6 magnitude (Figure S5 C and D). Using changes in  $^1\text{H}^{15}\text{N}$ -TROSY peak intensities on addition of  
7  $\text{Mg}^{\text{II}}$  to the  $\text{Mg}^{\text{II}}$ -free  $\beta\text{PGM}_{\text{D10N}}:\text{P1G6P}$  complex, the dissociation constant for  $\text{Mg}^{\text{II}}$  binding was  
8 determined to be  $7.1 \pm 0.6$  mM (Figure S7 B and C), consistent with the initial purification of the  
9  $\beta\text{PGM}_{\text{D10N}}:\text{P1G6P}$  complexes being a mixture of  $\text{Mg}^{\text{II}}$ -bound and  $\text{Mg}^{\text{II}}$ -free forms in the  
10 presence of 5 mM  $\text{MgCl}_2$ . In contrast, all metal fluoride analogue complexes of  $\beta\text{PGM}$  exist in  
11 solution as  $\text{Mg}^{\text{II}}$ -bound species at this concentration of  $\text{MgCl}_2$ . The changes in the  $^{31}\text{P}$  NMR  
12 chemical shifts between the  $\text{Mg}^{\text{II}}$ -bound and  $\text{Mg}^{\text{II}}$ -free  $\beta\text{PGM}_{\text{D10N}}:\text{P1G6P}$  complexes (1-  
13 phosphate = +0.71 ppm, 6-phosphate = -0.09 ppm) are small compared with those associated  
14 with protonation of  $\beta\text{G1P}$  (-3.4 ppm) or  $\text{G6P}$  (-3.6 ppm) (Figure 2A and Figure S1 F-K),  
15 indicating that  $\text{Mg}^{\text{II}}$  binding is not influenced significantly by protonation of either phosphate  
16 group. Rather, the surprisingly low affinity for  $\text{Mg}^{\text{II}}$  at this point on the reaction coordinate  
17 correlates with its sub-optimal coordination geometry in the structure of the  $\beta\text{PGM}_{\text{D10N}}:\text{P1G6P}$   
18 complex (Figure S7A), in contrast to the regular  $\text{Mg}^{\text{II}}$  coordination geometry observed in the  
19  $\beta\text{PGM}_{\text{D10N}}:\text{BeF}_3$  and  $\beta\text{PGM}_{\text{D10N}}:\text{AlF}_4:\text{G6P}$  TSA complex structures.  
20  
21  
22  
23  
24  
25  
26  
27  
28  
29  
30  
31  
32  
33  
34  
35  
36  
37  
38  
39  
40  
41  
42  
43  
44  
45  
46

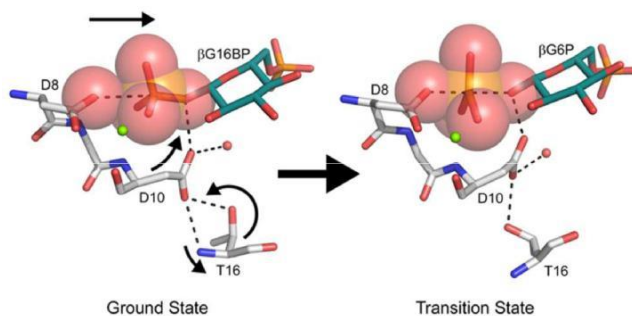
## 47 DISCUSSION

48  
49  
50 A unique behavior of the  $\beta\text{PGM}_{\text{D10N}}$  variant is that, unlike all other forms of  $\beta\text{PGM}$  examined  
51 to date, it co-purifies as tight, non-covalently bound  $\beta\text{PGM}_{\text{D10N}}:\beta\text{G16BP}$  complexes. Effective  
52 removal of the bound  $\beta\text{G16BP}$  reaction intermediate required an unfolding-dilution-refolding  
53  
54  
55  
56  
57  
58  
59  
60

1  
2  
3 approach. When challenged with substrate in the presence of excess AcP, the substrate-free  
4  
5  $\beta$ PGMD10N preparation equilibrates  $\beta$ G1P and G6P, with  $\beta$ PGMD10N<sup>P</sup> maintained as the primary  
6  
7 enzyme species. On depletion of AcP, the enzyme population shifts slowly to the  
8  
9  $\beta$ PGMD10N:P1G6P complex becoming the dominant species. In this complex, the 1-phosphate  
10  
11 group of  $\beta$ G16BP is aligned with the carboxylate oxygen atom of D8, and the sidechain of N10  
12  
13 is shifted to the *in* position, where it forms a hydrogen bond with the bridging 1-oxygen atom of  
14  
15  $\beta$ G16BP. The enzyme is now caught in the act of phosphoryl transfer, geometrically close to the  
16  
17 TS, but unable to complete the reaction (or at least overwhelmingly favoring the 1-phosphate  
18  
19 group being bonded to G6P), as N10 will not release the proton hydrogen bonded to the bridging  
20  
21 oxygen atom.  
22  
23  
24  
25  
26  
27  
28

29 The DFT calculations of  $\beta$ PGM<sub>WT</sub> reflect enzymatic phosphoryl transfer reactions in general  
30  
31 (25) in that the point at which proton transfer occurs is controversial. Two  $\beta$ PGM<sub>WT</sub> models  
32  
33 predict that, when D8 attacks  $\beta$ G16BP in Step 2, proton transfer to  $\beta$ G16BP occurs prior to TS  
34  
35 formation, and in the TS there is a donor to acceptor atom separation of 4.2 Å (11) or 4.4 Å (12).  
36  
37 In a third model, proton transfer is synchronous with TS formation involving a donor to acceptor  
38  
39 atom separation of 4.0 Å (56), while in a fourth model, proton transfer to  $\beta$ G16BP occurs after  
40  
41 TS formation, and in the TS there is a donor to acceptor atom separation of 5.0 Å (13). The  
42  
43 experiment supports the predictions of the first two models, as the  $\beta$ PGMD10N:P1G6P complex  
44  
45 rather than the  $\beta$ PGMD10N<sup>P</sup>:G6P complex is trapped and, without proton transfer, the donor to  
46  
47 acceptor atom separation is held at 4.6 Å. Intriguingly, in the 4.4 Å TS model (12), a  
48  
49 compression of the donor to acceptor atom separation to less than 4.6 Å is associated with the  
50  
51 start of proton transfer from D10 to  $\beta$ G16BP. Moreover, with the donor to acceptor atom  
52  
53  
54  
55  
56  
57  
58  
59  
60

1  
2  
3 separation being held 0.2 – 0.4 Å greater than that in the TS, the two domains of  $\beta$ PGM do not  
4  
5 complete their closure. Full closure, including the hydrogen bonding of T16 and N10/D10 found  
6  
7 in the TS, is only stable when there is compression of the reaction coordinate to below the van  
8  
9 der Waals contact distance, as mimicked by the TSA complexes ( $\text{AlF}_4^- = 3.9 \text{ \AA}$ , PDB 2WF6;  
10  
11  $\text{MgF}_3^- = 4.3 \text{ \AA}$ , PDB 2WF5 (20)) (Figure 4). Corroboration of the partial closure of the  
12  
13  $\beta$ PGM<sub>D10N</sub> complexes is also present in the solution ensembles, where residues of the hinge in  
14  
15 the  $\beta$ PGM<sub>D10N</sub>:PIG6P complex lie in an intermediate position between the open and the TSA  
16  
17 conformations, and residues D15 and T16 fail to achieve the hydrogen bond arrangement in the  
18  
19 TS model (Figure S9). Together, these observations illustrate the complementarity between the  
20  
21 TS and the optimal hydrogen bonding of the fully closed enzyme in the TSA conformation, as  
22  
23 TS and the optimal hydrogen bonding of the fully closed enzyme in the TSA conformation, as  
24  
25 opposed to the partially open ground state  $\beta$ G16BP complex, and thus a means by which the  
26  
27 enzyme discriminates between the TS (binding it tightly enough to have a sufficiently fast  
28  
29 chemical step) and product (binding it weakly enough that it does not dissociate too slowly).  
30  
31  
32  
33  
34  
35  
36  
37



38  
39  
40  
41  
42  
43  
44  
45  
46  
47  
48  
49 **Figure 4.** A schematic showing the conformational changes required for ground state to  
50  
51 transition state progression in  $\beta$ PGM. Despite van der Waals contact between the attacking  
52  
53 nucleophilic carboxylate oxygen atom of D8 and the 1-phosphorus atom of  $\beta$ G16BP in the  
54  
55  
56  
57  
58  
59  
60

1  
2  
3 ground state  $\beta$ PGM<sub>D10N</sub>:P1G6P complex (PDB 5OK1), the hydrogen bonding organization of  
4  
5  
6 the transition state is not attained. A shift in hydrogen bonding partners between T16 and D10 is  
7  
8 required to allow positional changes in both sidechains, which delivers the protonated general  
9  
10 acid-base to the bridging oxygen atom of  $\beta$ G16BP. Following proton transfer, further  
11  
12 compression along the donor-acceptor oxygen atom trajectory occurs, establishing the conformation  
13  
14 of the transition state (model derived from the  $\beta$ PGM<sub>WT</sub>:MgF<sub>3</sub>:G6P TSA complex;  
15  
16 PDB 2WF5 (20)). Selected active site residues and ligands are shown as sticks in standard CPK  
17  
18 colors, with a structural water (red) and the catalytic Mg<sup>II</sup> ion (green) drawn as spheres. Large  
19  
20 translucent spheres represent van der Waals radii for the oxygen and phosphorus atoms of the  
21  
22 transferring phosphoryl group.  
23  
24  
25  
26  
27  
28  
29

30 The rate constant for hydrolysis of the phospho-enzyme is almost unaffected by the D10N  
31  
32 mutation. This result is readily rationalized if hydrolysis occurs with residue 10 in the *out*  
33  
34 position, as observed for N10 in the  $\beta$ PGM<sub>D10N</sub>:BeF<sub>3</sub> complex (PDB 5OJZ) and D10 in the  
35  
36  $\beta$ PGM<sub>WT</sub>:BeF<sub>3</sub> complex (PDB 2WFA (23)). Previously, it had been proposed that D10 was  
37  
38 engaged in the hydrolysis reaction of  $\beta$ PGM<sub>WT</sub><sup>P</sup> on the basis of a rate acceleration by the mutated  
39  
40 hinge variant  $\beta$ PGM<sub>T16P</sub> (8). However, this mechanism is not dominant in  $\beta$ PGM<sub>WT</sub>; the water  
41  
42 molecule that attacks the phosphate group during hydrolysis must at least as readily transfer a  
43  
44 proton to an ancillary base as to residue 10. The identity of the ancillary base remains to be  
45  
46 established but the oxygen atoms of the transferring phosphoryl group (*via* one or more water  
47  
48 molecules) are strong local candidates. However, the base may be another residue in  $\beta$ PGM<sub>WT</sub>  
49  
50  
51 (except for residue H20 (8)) or the buffer, *via* extended hydrogen bonded networks involving  
52  
53 multiple water molecules.  
54  
55  
56  
57  
58  
59  
60

1  
2  
3  
4  
5 While the  $\beta\text{PGM}_{\text{D10N}}^{\text{P}}$  hydrolysis rate constant cannot be rationalized by a contaminant within  
6 the substrate-free  $\beta\text{PGM}_{\text{D10N}}$  preparation,  $\beta\text{PGM}_{\text{D10N}}$  is not unequivocally the source of the  
7 observed mutase activity. However, similarly to the phospho-enzyme hydrolysis reaction, it is  
8 plausible that proton transfer to the incipient hydroxyl group of G6P or  $\beta\text{G1P}$  (as the 1- or 6-  
9 phosphoryl group of  $\beta\text{G16BP}$  transfers to residue D8) is delivered from an ancillary acid by a  
10 water molecule. In a model of the  $\beta\text{PGM}_{\text{D10N}}:\text{P1G6P}$  complex with N10 moved to the *out*  
11 position (Figure S10), the two water molecules that occupy the space vacated by the sidechain of  
12 N10 comprise part of an extended hydrogen bonded network, involving active site residues H20,  
13 K76, Y80 and the phosphate group in the *distal* site, and reaching to bulk solvent. Any one of  
14 these groups or the buffer (or even potentially the phosphate group in the *proximal* site) could act  
15 as the ancillary acid *via* one or more water molecules, allowing low level mutase activity to  
16 occur in  $\beta\text{PGM}_{\text{D10N}}$ .  
17  
18  
19  
20  
21  
22  
23  
24  
25  
26  
27  
28  
29  
30  
31  
32  
33  
34  
35

36 Regardless of the source of the mutase activity, the replacement of D10 with N10 leads to at  
37 least a  $\sim 350$  fold (Figure S3 I and J) reduction in activity. Consequently, the primary effect of  
38 introducing the general acid-base into  $\beta\text{PGM}_{\text{WT}}$  is to elevate the rate of substrate turnover to  
39  $\sim 10^3$  fold (Figure S3 C and I) greater than the rate of phospho-enzyme hydrolysis, enabling the  
40 enzyme to discriminate reaction with substrate over reaction with water. This ensures that  $\beta\text{PGM}$   
41 is primarily a mutase rather than a phosphatase.  
42  
43  
44  
45  
46  
47  
48  
49  
50  
51

52 The co-purified  $\beta\text{PGM}_{\text{D10N}}:\beta\text{G16BP}$  complexes are present as a near-equimolar mixture of  
53  $\text{Mg}^{\text{II}}$ -bound and  $\text{Mg}^{\text{II}}$ -free  $\beta\text{PGM}_{\text{D10N}}:\text{P1G6P}$  complexes in standard NMR buffer (5 mM  $\text{Mg}^{\text{II}}$ ).  
54  
55  
56  
57  
58  
59  
60



1  
2  
3 This reflects the surprisingly low affinity of these complexes for  $\text{Mg}^{\text{II}}$  ( $K_{\text{d}} = 7.1 \text{ mM}$ ) compared  
4  
5 with the apparent  $K_{\text{m}} = 270 \text{ }\mu\text{M}$  for  $\text{Mg}^{\text{II}}$  in the reaction involving  $\beta\text{PGM}_{\text{WT}}$  (17), and is similar  
6  
7 to the physiological concentration of  $\text{Mg}^{\text{II}}$  for *L. lactis* (~7 mM (57)). The conclusion is that  
8  
9  $\beta\text{G16BP}$  binding leads to a sub-optimally coordinated catalytic  $\text{Mg}^{\text{II}}$  ion until full closure is  
10  
11 achieved. More optimal coordination of the catalytic  $\text{Mg}^{\text{II}}$  ion is found in structures that include  
12  
13 the 0.2 – 0.4 Å reduction in donor to acceptor atom separation associated with the formation of  
14  
15 experimental TSA complexes and in DFT models of the TS. In a different class of phosphoryl  
16  
17 transfer enzymes, the catalytic  $\text{Mg}^{\text{II}}$  ion has been identified to play a role in the rate of lid  
18  
19 opening during the reaction cycle of adenylate kinase (58), as well as reducing non-productive  
20  
21 active site fluctuations, stabilizing TS architecture, and serving as an anchor to stabilize the  
22  
23 nucleophilic phosphate group. In  $\beta\text{PGM}$ , rather than acting as a pivot for opening, it appears that  
24  
25 the catalytic  $\text{Mg}^{\text{II}}$  ion is favoring TS binding and disfavoring substrate binding by forming a  
26  
27 looser association with its ligands as the TS relaxes to ground state complexes.  
28  
29  
30  
31  
32  
33  
34  
35  
36

## 37 CONCLUSIONS

38  
39  
40 The employment of an aspartate to asparagine substitution of the assigned general acid-base of  
41  
42  $\beta\text{PGM}$  allowed the examination of stable enzyme:substrate complexes through the ability of  
43  
44  $\beta\text{PGM}_{\text{D10N}}$  to trap the  $\beta\text{G16BP}$  reaction intermediate *in situ*. Unlike previous structures  
45  
46 determined for substrate, transition state, and product analogue complexes involving  $\beta\text{G1P}$  and  
47  
48  $\text{G6P}$ , the  $\beta\text{G16BP}$  complex achieves both alignment and contact of the attacking nucleophile  
49  
50 with its target but without full closure of the enzyme. This reveals the interplay between  
51  
52 compression of the reaction coordinate to below the van der Waals contact distance and the  
53  
54  
55  
56  
57  
58  
59  
60

1  
2  
3 protein conformation that supports the transition state for the chemical step. The coordination of  
4  
5 the catalytic  $\text{Mg}^{\text{II}}$  ion is an important element of this interplay on the one hand by  
6  
7 complementing the transition state and on the other by facilitating the release of the reaction  
8  
9 intermediate on an appropriate timescale.  
10  
11  
12  
13  
14  
15  
16  
17  
18

## 19 ASSOCIATED CONTENT

### 22 **Supporting Information**

23  
24  
25 The Supporting Information is available free of charge on the ACS Publications website at DOI:

26  
27  
28  
29  $^{31}\text{P}$ ,  $^1\text{H}^{13}\text{C}$  HSQC and  $^1\text{H}^{15}\text{N}$  TROSY NMR spectra;  $\beta\text{PGM}$  reaction kinetics, electron density  
30  
31 difference and omit maps for the  $\beta\text{PGM}_{\text{D10N}}$  complexes; diagrams of chemical shift differences  
32  
33 and backbone dihedral angles; superposition of the  $\beta\text{PGM}_{\text{D10N}}:\text{P1G6P}$  complexes; coordination  
34  
35 and binding affinity of the catalytic  $\text{Mg}^{\text{II}}$  ion in the  $\beta\text{PGM}_{\text{D10N}}:\text{P1G6P}$  complex; active site  
36  
37 coordination in the  $\beta\text{PGM}_{\text{D10N}}:\beta\text{G16BP}$  complexes; comparison of backbone amide chemical  
38  
39 shifts in the  $\beta\text{PGM}_{\text{D10N}}$  complexes; model of the potentially catalytically competent form of the  
40  
41  $\beta\text{PGM}_{\text{D10N}}:\beta\text{P1G6P}$  complex; tables of X-ray data collection and refinement statistics, and  
42  
43 pairwise domain rotations between the  $\beta\text{PGM}$  complexes (PDF).  
44  
45  
46  
47  
48  
49

### 50 **Accession Codes**

51  
52  
53 The atomic coordinates and structure factors have been deposited in the Protein Data Bank  
54  
55 ([www.rcsb.org](http://www.rcsb.org)) with the following codes:  $\beta\text{PGM}_{\text{D10N}}:\text{BeF}_3$  complex (PDB 5OJZ),  
56  
57  
58  
59  
60

1  
2  
3  $\beta$ PGMD<sub>10N</sub>:P1G6P complex (PDB 5OK1), co-purified  $\beta$ PGMD<sub>10N</sub>:P1G6P complex (PDB 5O6P),  
4  
5  
6  $\beta$ PGMD<sub>10N</sub>:P6G1P complex (PDB 5OK0),  $\beta$ PGMD<sub>10N</sub>:AlF<sub>4</sub>:G6P complex (PDB 5OK2) and  
7  
8  $\beta$ PGMD<sub>10N</sub>:AlF<sub>4</sub>:H<sub>2</sub>O: $\beta$ G1P complex (PDB 5O6R). The NMR chemical shifts have been  
9  
10 deposited in the BioMagResBank ([www.bmrb.wisc.edu](http://www.bmrb.wisc.edu)) with the following accession numbers:  
11  
12  
13 Mg<sup>II</sup>-bound  $\beta$ PGMD<sub>10N</sub>:P1G6P complex (BMRB 27174) and Mg<sup>II</sup>-free  $\beta$ PGMD<sub>10N</sub>:P1G6P  
14  
15 complex (BMRB 27175).  
16  
17  
18  
19

## 20 AUTHOR INFORMATION

### 21 22 23 **Corresponding Author**

24  
25  
26 \* E-mail for J.P.W.: [j.waltho@sheffield.ac.uk](mailto:j.waltho@sheffield.ac.uk)  
27  
28

### 29 **ORCID**

30  
31 Jonathan Waltho: 0000-0002-7402-5492  
32  
33

### 34 35 **Present Addresses**

36  
37 <sup>‡</sup>(L.A.J. and Y.J.) School of Chemistry, Cardiff University, Cardiff, CF10 3AT, United  
38  
39 Kingdom  
40  
41

42  
43 <sup>§</sup>(C.B.) Institute of Structural and Molecular Biology, Department of Biological Sciences,  
44  
45 Birkbeck, University of London, London, WC1E 7HX, United Kingdom  
46  
47

### 48 **Author Contributions**

49  
50 <sup>#</sup>(L.A.J. and A.J.R.) These authors contributed equally.  
51  
52

### 53 **Notes**

54  
55  
56  
57  
58  
59  
60

1  
2  
3 The authors declare no competing financial interest.  
4  
5  
6  
7  
8  
9  
10

11  
12  
13 ACKNOWLEDGMENTS  
14

15  
16 We would like to thank Dr Tooba Alizadeh for the preparation of the  $\beta$ PGM<sub>D10N</sub> plasmid  
17  
18 construct and for the acquisition and interpretation of preliminary NMR experiments. We would  
19  
20 also like to thank the beamline scientists at the Diamond Light Source (DLS) and the European  
21  
22 Synchrotron Radiation Facility (ESRF) for the provision of synchrotron radiation facilities and  
23  
24 assistance with data collection. This research was supported by the Biotechnology and Biological  
25  
26 Sciences Research Council (N.J.B. – grant number: BB/M021637/1; C.T. – grant number:  
27  
28 BB/K016245/1) and the Engineering and Physical Sciences Research Council (NMR  
29  
30 spectrometer core capability – grant number: EP/K039547/1).  
31  
32  
33  
34  
35  
36  
37

38 REFERENCES  
39

- 40 (1) Hunter, T. Why Nature Chose Phosphate to Modify Proteins. *Phil. Trans. R. Soc. B* **2012**,  
41  
42 *367*, 2513–2516.  
43  
44  
45 (2) Lad, C.; Williams, N. H.; Wolfenden, R. The Rate of Hydrolysis of Phosphomonoester  
46  
47 Dianions and the Exceptional Catalytic Proficiencies of Protein and Inositol Phosphatases. *Proc.*  
48  
49 *Natl. Acad. Sci. U. S. A.* **2003**, *100*, 5607–5610.  
50  
51  
52  
53 (3) Buechler, J. A.; Taylor, S. S. Identification of Aspartate-184 as an Essential Residue in the  
54  
55 Catalytic Subunit of cAMP-Dependent Protein Kinase. *Biochemistry* **1988**, *27*, 7356–7361.  
56  
57  
58  
59  
60

1  
2  
3 (4) Green, P. C.; Tripathi, R. L.; Kemp, R. G. Identification of Active Site Residues in  
4 Pyrophosphate-Dependent Phosphofructo-1-Kinase by Site-Directed Mutagenesis. *J. Biol. Chem.*  
5 **1993**, *268*, 5085–5088.  
6  
7

8  
9  
10 (5) Denu, J. M.; Lohse, D. L.; Vijayalakshmi, J.; Saper, M. A.; Dixon, J. E. Visualization of  
11 Intermediate and Transition-State Structures in Protein-Tyrosine Phosphatase Catalysis. *Proc.*  
12 *Natl. Acad. Sci. U. S. A.* **1996**, *93*, 2493–2498.  
13  
14  
15

16 (6) Wu, L.; Zhang, Z.-Y. Probing the Function of Asp128 in the Lower Molecular Weight  
17 Protein-Tyrosine Phosphatase-Catalyzed Reaction. A Pre-Steady-State and Steady-State Kinetic  
18 Investigation. *Biochemistry* **1996**, *35*, 5426–5434.  
19  
20  
21  
22  
23

24 (7) Skamnaki, V. T.; Owen, D. J.; Nobel, M. E. M.; Lowe, E. D.; Lowe, G.; Oikonomakos, N.  
25 G.; Johnson, L. N. Catalytic Mechanism of Phosphorylase Kinase Probed by Mutational Studies.  
26 *Biochemistry* **1999**, *38*, 14718–14730.  
27  
28  
29  
30  
31  
32

33 (8) Dai, J.; Finci, L.; Zhang, C.; Lahiri, S.; Zhang, G.; Peisach, E.; Allen, K. N.; Dunaway-  
34 Mariano, D. Analysis of the Structural Determinants Underlying Discrimination Between  
35 Substrate and Solvent in  $\beta$ -Phosphoglucomutase Catalysis. *Biochemistry* **2009**, *48*, 1984–1995.  
36  
37  
38  
39  
40  
41

42 (9) Valiev, M.; Kawai, R.; Adams, J. A.; Weare, J. H. The Role of the Putative Catalytic Base  
43 in the Phosphoryl Transfer Reaction in a Protein Kinase: First-Principles Calculations. *J. Am.*  
44 *Chem. Soc.* **2003**, *125*, 9926–9927.  
45  
46  
47  
48  
49

50 (10) Asthagiri, D.; Liu, T.; Noodleman, L.; Van Etten, R. L.; Bashford, D. On the Role of the  
51 Conserved Aspartate in the Hydrolysis of the Phosphocysteine Intermediate of the Low  
52 Molecular Weight Tyrosine Phosphatase. *J. Am. Chem. Soc.* **2004**, *126*, 12677–12684.  
53  
54  
55  
56  
57  
58  
59  
60

1  
2  
3 (11) Webster, C. E. High-Energy Intermediate or Stable Transition State Analogue: Theoretical  
4 Perspective of the Active Site and Mechanism of  $\beta$ -Phosphoglucomutase. *J. Am. Chem. Soc.*  
5  
6  
7 **2004**, *126*, 6840–6841.

8  
9  
10  
11 (12) Marcos, E.; Field, M. J.; Crehuet, R. Pentacoordinated Phosphorus Revisited by High-  
12  
13 Level QM/MM Calculations. *Proteins* **2010**, *78*, 2405–2411.

14  
15  
16  
17 (13) Elsässer, B.; Dohmeier-Fischer, S.; Fels, G. Theoretical Investigation of the Enzymatic  
18  
19 Phosphoryl Transfer of  $\beta$ -Phosphoglucomutase: Revisiting Both Steps of the Catalytic Cycle. *J.*  
20  
21 *Mol. Model.* **2012**, *18*, 3169–3179.

22  
23  
24  
25 (14) Kim, K.; Cole, P. A. Measurement of a Brønsted Nucleophile Coefficient and Insights  
26  
27 into the Transition State for a Protein Tyrosine Kinase. *J. Am. Chem. Soc.* **1997**, *119*,  
28  
29 11096–11097.

30  
31  
32  
33 (15) Zhou, J.; Adams, J. A. Is There a Catalytic Base in the Active Site of cAMP-Dependent  
34  
35 Protein Kinase? *Biochemistry* **1997**, *36*, 2977–2984.

36  
37  
38  
39 (16) Kim, K.; Cole, P. A. Kinetic Analysis of a Protein Tyrosine Kinase Reaction Transition  
40  
41 State in the Forward and Reverse Directions. *J. Am. Chem. Soc.* **1998**, *120*, 6851–6858.

42  
43  
44 (17) Zhang, G.; Dai, J.; Wang, L.; Dunaway-Mariano, D.; Tremblay, L. W.; Allen, K. N.  
45  
46 Catalytic Cycling in  $\beta$ -Phosphoglucomutase: A Kinetic and Structural Analysis. *Biochemistry*  
47  
48 **2005**, *44*, 9404–9416.

1  
2  
3 (18) Dai, J.; Wang, L.; Allen, K. N.; Radstrom, P.; Dunaway-Mariano, D. Conformational  
4  
5 Cycling in  $\beta$ -Phosphoglucomutase Catalysis: Reorientation of the  $\beta$ -D-Glucose 1,6-  
6  
7 (Bis)phosphate Intermediate. *Biochemistry* **2006**, *45*, 7818–7824.  
8  
9

10  
11 (19) Jin, Y.; Bhattasali, D.; Pellegrini, E.; Forget, S. M.; Baxter, N. J.; Cliff, M. J.; Bowler, M.  
12  
13 W.; Jakeman, D. L.; Blackburn, G. M.; Waltho, J. P.  $\alpha$ -Fluorophosphonates Reveal How a  
14  
15 Phosphomutase Conserves Transition State Conformation Over Hexose Recognition in Its Two-  
16  
17 Step Reaction. *Proc. Natl. Acad. Sci. U. S. A.* **2014**, *111*, 12384–12389.  
18  
19

20  
21 (20) Baxter, N. J.; Bowler, M. W.; Alizadeh, T.; Cliff, M. J.; Hounslow, A. M.; Wu, B.;  
22  
23 Berkowitz, D. B.; Williams, N. H.; Blackburn, G. M.; Waltho, J. P. Atomic Details of Near-  
24  
25 Transition State Conformers for Enzyme Phosphoryl Transfer Revealed by  $\text{MgF}_3^-$  Rather Than  
26  
27 by Phosphoranes. *Proc. Natl. Acad. Sci. U. S. A.* **2010**, *107*, 4555–4560.  
28  
29

30  
31 (21) Baxter, N. J.; Olguin, L. F.; Goličnik, M.; Feng, G.; Hounslow, A. M.; Bermel, W.;  
32  
33 Blackburn, G. M.; Hollfelder, F.; Waltho, J. P.; Williams, N. H. A Trojan Horse Transition State  
34  
35 Analogue Generated by  $\text{MgF}_3^-$  Formation in an Enzyme Active Site. *Proc. Natl. Acad. Sci. U. S.*  
36  
37 *A.* **2006**, *103*, 14732–14737.  
38  
39

40  
41 (22) Baxter, N. J.; Hounslow, A. M.; Bowler, M. W.; Williams, N. H.; Blackburn, G. M.;  
42  
43 Waltho, J. P.  $\text{MgF}_3^-$  and  $\alpha$ -Galactose 1-Phosphate in the Active Site of  $\beta$ -Phosphoglucomutase  
44  
45 Form a Transition State Analogue of Phosphoryl Transfer. *J. Am. Chem. Soc.* **2009**, *131*,  
46  
47 16334–16335.  
48  
49

50  
51 (23) Griffin, J. L.; Bowler, M. W.; Baxter, N. J.; Leigh, K. N.; Dannatt, H. R. W.; Hounslow,  
52  
53 A. M.; Blackburn, G. M.; Webster, C. E.; Cliff, M. J.; Waltho, J. P. Near Attack Conformers  
54  
55  
56  
57  
58  
59  
60

1  
2  
3 Dominate  $\beta$ -Phosphoglucomutase Complexes Where Geometry and Charge Distribution Reflect  
4 Those of Substrate. *Proc. Natl. Acad. Sci. U. S. A.* **2012**, *109*, 6910–6915.  
5  
6  
7

8  
9 (24) Jin, Y.; Richards, N. G. J.; Waltho, J. P.; Blackburn, G. M. Metal Fluorides as Analogues  
10 for Studies on Phosphoryl Transfer Enzymes. *Angew. Chem. Int. Ed.* **2017**, *56*, 4110–4128.  
11  
12

13  
14 (25) Jin, Y.; Molt, R. W.; Blackburn, G. M. Metal Fluorides: Tools for Structural and  
15 Computational Analysis of Phosphoryl Transfer Enzymes. *Top. Curr. Chem.* **2017**, *375*, 36–59.  
16  
17

18  
19 (26) Bruice, T. C. Some Pertinent Aspects of Mechanism as Determined With Small  
20 Molecules. *Annu. Rev. Biochem.* **1976**, *45*, 331–374.  
21  
22

23  
24 (27) Jin, Y.; Molt, R. W.; Waltho, J. P.; Richards, N. G. J.; Blackburn, G. M.  $^{19}\text{F}$  NMR and  
25 DFT Analysis Reveal Structural and Electronic Transition State Features for RhoA-Catalyzed  
26 GTP Hydrolysis. *Angew. Chem. Int. Ed.* **2016**, *55*, 3318–3322.  
27  
28

29  
30 (28) Jin, Y.; Molt, R. W.; Pellegrini, E.; Cliff, M. J.; Bowler, M. W.; Richards, N. G. J.;  
31 Blackburn, G. M.; Waltho, J. P. Assessing the Influence of Mutation on GTPase Transition  
32 States Using X-Ray Crystallography,  $^{19}\text{F}$  NMR and DFT Approaches. *Angew. Chem. Int. Ed.*  
33  
34  
35  
36  
37  
38  
39  
40  
41 **2017**, *56*, 9732–9735.  
42

43  
44 (29) Reed, M. A. C.; Hounslow, A. M.; Sze, K. H.; Barsukov, I. G.; Hosszu, L. L. P.; Clarke,  
45 A. R.; Craven, C. J.; Waltho, J. P. Effects of Domain Dissection on the Folding and Stability of  
46 the 43 kDa Protein PGK Probed by NMR. *J. Mol. Biol.* **2003**, *330*, 1189–1201.  
47  
48  
49  
50  
51  
52  
53  
54  
55  
56  
57  
58  
59  
60



1  
2  
3 (30) Goličnik, M.; Olguin, L. F.; Feng, G.; Baxter, N. J.; Waltho, J. P.; Williams, N. H.;  
4  
5 Hollfelder, F. Kinetic Analysis of  $\beta$ -Phosphoglucomutase and Its Inhibition by Magnesium  
6  
7 Fluoride. *J. Am. Chem. Soc.* **2009**, *131*, 1575–1588.  
8  
9

10  
11 (31) Vranken, W. F.; Boucher, W.; Stevens, T. J.; Fogh, R. H.; Pajon, A.; Llinas, M.; Ulrich, E.  
12  
13 L.; Markley, J. L.; Ionides, J.; Laue, E. D. The CCPN Data Model for NMR Spectroscopy:  
14  
15 Development of a Software Pipeline. *Proteins* **2005**, *59*, 687–696.  
16  
17

18  
19 (32) Schulte-Herbrüggen, T.; Sørensen, O. W. Clean TROSY: Compensation for Relaxation-  
20  
21 Induced Artefacts. *J. Magn. Reson.* **2000**, *144*, 123–128.  
22  
23

24  
25 (33) Lescop, E.; Schanda, P.; Brutscher, B. A Set of BEST Triple-Resonance Experiments for  
26  
27 Time-Optimized Protein Resonance Assignment. *J. Magn. Reson.* **2007**, *187*, 163–169.  
28  
29

30  
31 (34) Hyberts, S. G.; Robson, S. A.; Wagner, G. Exploring Signal-to-Noise Ratio and  
32  
33 Sensitivity in Non-Uniformly Sampled Multi-Dimensional NMR Spectra. *J. Biomol. NMR* **2013**,  
34  
35 *55*, 167–178.  
36  
37

38  
39 (35) Hyberts, S. G.; Milbradt, A. G.; Wagner, A. B.; Arthanari, H.; Wagner, G. Application of  
40  
41 Iterative Soft Thresholding for Fast Reconstruction of NMR Data Non-Uniformly Sampled With  
42  
43 Multidimensional Poisson Gap Scheduling. *J. Biomol. NMR* **2012**, *52*, 315–327.  
44  
45

46  
47 (36) Sun, Z.-Y. J.; Frueh, D. P.; Selenko, P.; Hoch, J. C.; Wagner, G. Fast Assignment of  $^{15}\text{N}$ -  
48  
49 HSQC Peaks Using High-Resolution 3D HNCocaNH Experiments With Non-Uniform Sampling.  
50  
51 *J. Biomol. NMR* **2005**, *33*, 43–50.  
52  
53  
54  
55  
56  
57  
58  
59  
60

- 1  
2  
3 (37) Williamson, M. P. Using Chemical Shift Perturbation to Characterise Ligand Binding.  
4  
5 *Prog. Nucl. Magn. Reson. Spectrosc.* **2013**, *73*, 1–16.  
6  
7  
8 (38) Pellegrini, E.; Piano, D.; Bowler, M. W. Direct Cryocooling of Naked Crystals: Are  
9 Cryoprotection Agents Always Necessary? *Acta Cryst.* **2011**, *D67*, 902–906.  
10  
11  
12 (39) Winter, G. *xia2*: An Expert System for Macromolecular Crystallography Data Reduction.  
13  
14 *J. Appl. Cryst.* **2010**, *43*, 186–190.  
15  
16  
17 (40) Battye, T. G. G.; Kontogiannis, L.; Johnson, O.; Powell, H. R.; Leslie, A. G. W.  
18  
19 iMOSFLM: A New Graphical Interface for Diffraction-Image Processing With MOSFLM. *Acta*  
20  
21  
22  
23  
24  
25  
26  
27  
28 (41) Vagin, A.; Teplyakov, A. MOLREP: An Automated Program for Molecular Replacement.  
29  
30  
31  
32 *J. Appl. Cryst.* **1997**, *30*, 1022–1025.  
33  
34 (42) Emsley, P.; Lohkamp, B.; Scott, W. G.; Cowtan, K. Features and Development of COOT.  
35  
36  
37  
38  
39  
40  
41  
42  
43  
44 (43) Murshudov, G. N.; Vagin, A. A.; Dodson, E. J. Refinement of Macromolecular Structures  
45  
46  
47  
48  
49  
50  
51  
52  
53  
54  
55  
56  
57  
58  
59  
60  
by the Maximum-Likelihood Method. *Acta Cryst.* **1997**, *D53*, 240–255.  
  
54 (44) Chen, V. B.; Arendall, W. B.; Headd, J. J.; Keedy, D. A.; Immormino, R. M.; Kapral, G.  
55  
56  
57  
58  
59  
60  
J.; Murray, L. W.; Richardson, J. S.; Richardson, D. C. MolProbity: All-Atom Structure  
Validation for Macromolecular Crystallography. *Acta Cryst.* **2010**, *D66*, 12–21.  
  
54 (45) The PyMOL Molecular Graphics System, Version 1.8. (Schrödinger, LLC, 2015).

1  
2  
3 (46) Read, R. J.; Schierbeek, A. J. A Phased Translation Function. *J. Appl. Cryst.* **1988**, *21*,  
4  
5 490–495.  
6

7  
8  
9 (47) Hayward, S.; Berendsen, H. J. C. Systematic Analysis of Domain Motions in Proteins  
10 From Conformational Change: New Results on Citrate Synthase and T4 Lysozyme. *Proteins*  
11 **1998**, *30*, 144–154.  
12  
13

14  
15  
16 (48) Lahiri, S. D.; Zhang, G.; Radstrom, P.; Dunaway-Mariano, D.; Allen, K. N.  
17 Crystallization and Preliminary X-Ray Diffraction Studies of  $\beta$ -Phosphoglucomutase From  
18 *Lactococcus lactis*. *Acta Cryst.* **2002**, *D58*, 324–326.  
19  
20  
21

22  
23  
24 (49) Lahiri, S. D.; Zhang, G.; Dunaway-Mariano, D.; Allen, K. N. Caught in the Act: The  
25 Structure of Phosphorylated  $\beta$ -Phosphoglucomutase From *Lactococcus lactis*. *Biochemistry*  
26 **2002**, *41*, 8351–8359.  
27  
28  
29

30  
31  
32 (50) Lahiri, S. D.; Zhang, G.; Dunaway-Mariano, D.; Allen, K. N. The Pentavalent  
33 Phosphorus Intermediate of a Phosphoryl Transfer Reaction. *Science* **2003**, *299*, 2067–2071.  
34  
35  
36

37  
38 (51) Tyler-Cross, R.; Schirch, V. Effects of Amino Acid Sequence, Buffers, and Ionic Strength  
39 on the Rate and Mechanism of Deamidation of Asparagine Residues in Small Peptides. *J. Biol.*  
40 *Chem.* **1991**, *266*, 22549–22556.  
41  
42  
43

44  
45  
46 (52) Rowland, R. S.; Taylor, R. Intermolecular Nonbonded Contact Distances in Organic  
47 Crystal Structures: Comparison With Distances Expected From van der Waals Radii. *J. Phys.*  
48 *Chem.* **1996**, *100*, 7384–7391.  
49  
50  
51  
52  
53  
54  
55  
56  
57  
58  
59  
60

1  
2  
3 (53) Baxter, N. J.; Blackburn, G. M.; Marston, J. P.; Hounslow, A. M.; Cliff, M. J.; Bermel,  
4 W.; Williams, N. H.; Hollfelder, F.; Wemmer, D. E.; Waltho, J. P. Anionic Charge Is Prioritized  
5 Over Geometry in Aluminum and Magnesium Fluoride Transition State Analogs of Phosphoryl  
6 Transfer Enzymes. *J. Am. Chem. Soc.* **2008**, *130*, 3952–3958.  
7  
8  
9

10  
11  
12  
13 (54) Woolley, E. M.; Tomkins, J.; Hepler, L. G. Ionization Constants for Very Weak Organic  
14 Acids in Aqueous Solution and Apparent Ionization Constants for Water in Aqueous Organic  
15 Mixtures. *J. Solution Chem.* **1972**, *1*, 341–351.  
16  
17  
18  
19

20  
21 (55) Shen, Y.; Bax, A. Protein Backbone and Sidechain Torsion Angles Predicted From NMR  
22 Chemical Shifts Using Artificial Neural Networks. *J. Biomol. NMR* **2013**, *56*, 227–241.  
23  
24  
25

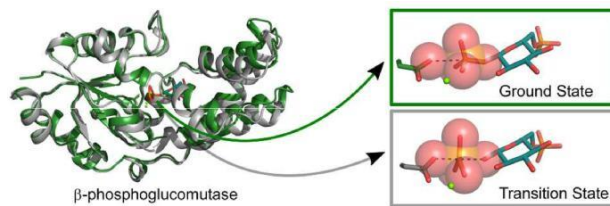
26  
27 (56) Barrozo, A.; Liao, Q.; Esguerra, M.; Marloie, G.; Florian, J.; Williams, N. H.; Kamerlin,  
28 S. C. L. Computer Simulations of the Catalytic Mechanism of Wild-Type and Mutant  $\beta$ -  
29 Phosphoglucomutase. *Org. Biomol. Chem.* **2018**, *16*, 2060–2073.  
30  
31  
32  
33

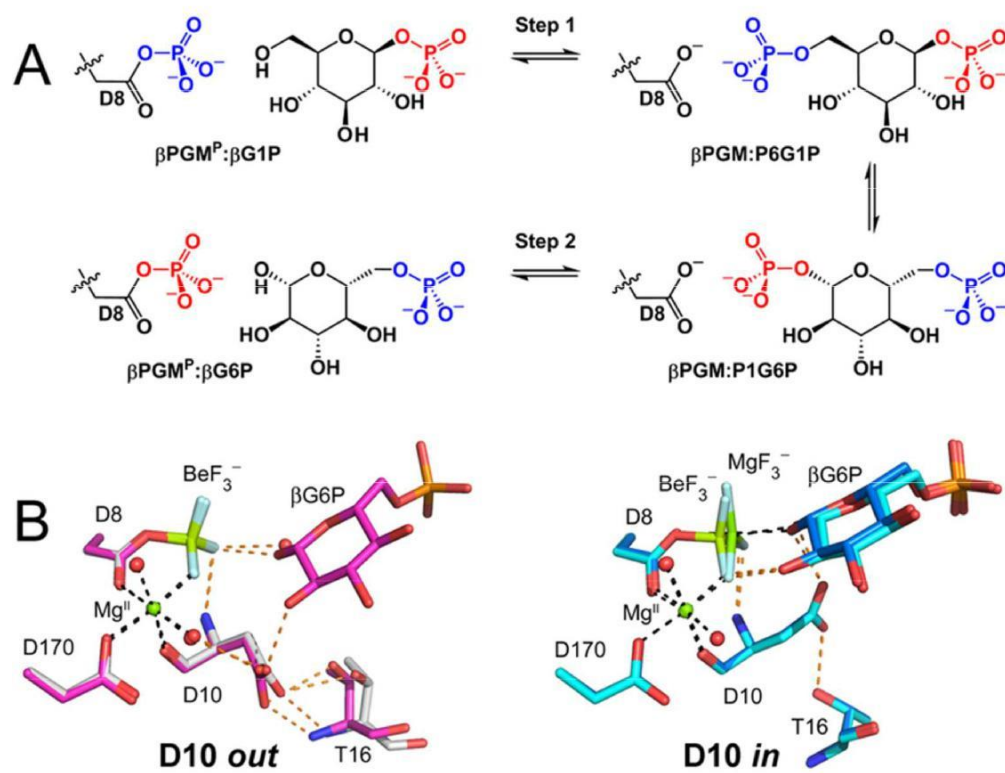
34 (57) Zamberlin, Š.; Antunac, N.; Havranek, J.; Samaržija, D. Mineral Elements in Milk and  
35 Dairy Products. *Mljekarstvo* **2012**, *62*, 111–125.  
36  
37  
38  
39

40 (58) Kerns, S. J.; Agafonov, R. V.; Cho, Y.-J.; Pontiggia, F.; Otten, R.; Pachov, D. V.; Kutter,  
41 S.; Phung, L. A.; Murphy, P. N.; Thai, V.; Alber, T.; Hagan, M. F.; Kern, D. The Energy  
42 Landscape of Adenylate Kinase During Catalysis. *Nat. Struct. Mol. Biol.* **2015**, *22*, 124–131.  
43  
44  
45  
46  
47  
48  
49  
50  
51  
52  
53  
54  
55  
56  
57  
58  
59  
60

1  
2  
3  
4  
5  
6  
7  
8  
9  
10  
11  
12  
13  
14  
15  
16  
17  
18  
19  
20  
21  
22  
23  
24  
25  
26  
27  
28  
29  
30  
31  
32  
33  
34  
35  
36  
37  
38  
39  
40  
41  
42  
43  
44  
45  
46  
47  
48  
49  
50  
51  
52  
53  
54  
55  
56  
57  
58  
59  
60

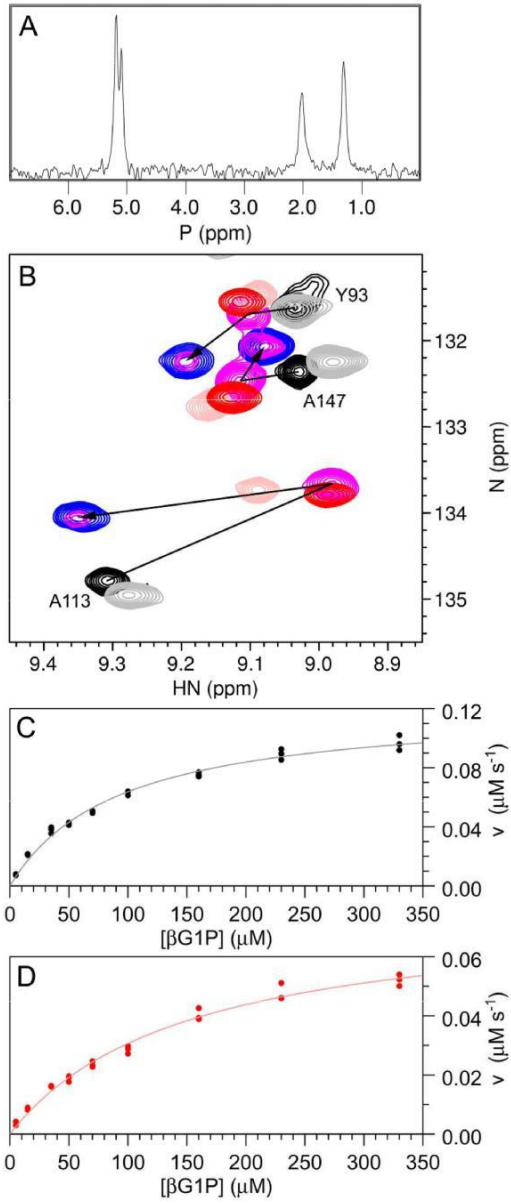
TOC GRAPHIC



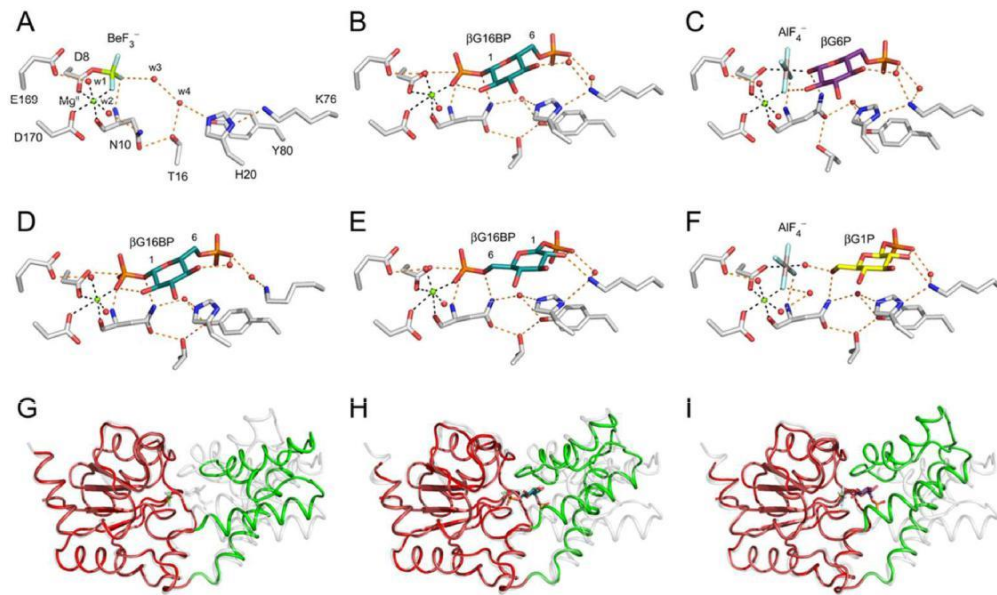


68x53mm (300 x 300 DPI)

1  
2  
3  
4  
5  
6  
7  
8  
9  
10  
11  
12  
13  
14  
15  
16  
17  
18  
19  
20  
21  
22  
23  
24  
25  
26  
27  
28  
29  
30  
31  
32  
33  
34  
35  
36  
37  
38  
39  
40  
41  
42  
43  
44  
45  
46  
47  
48  
49  
50  
51  
52  
53  
54  
55  
56  
57  
58  
59  
60

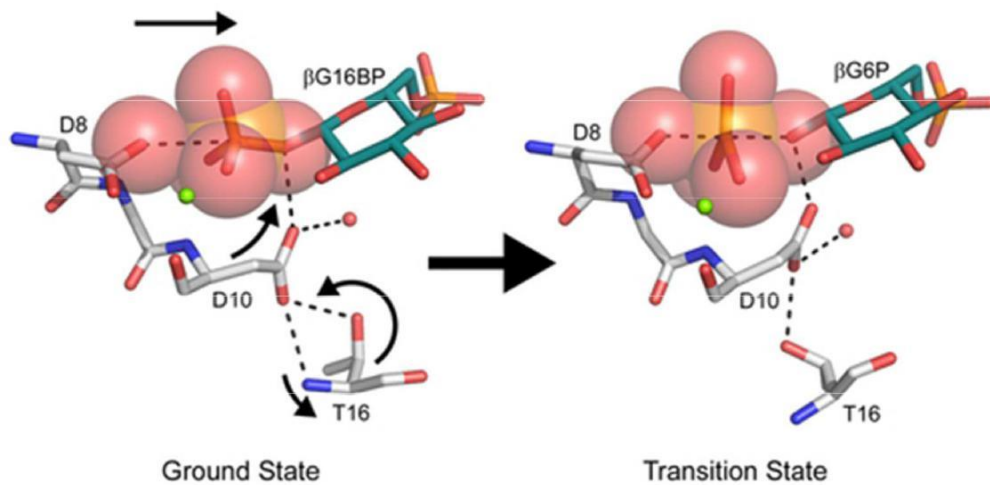


204x480MM (300 x 300 DPI)



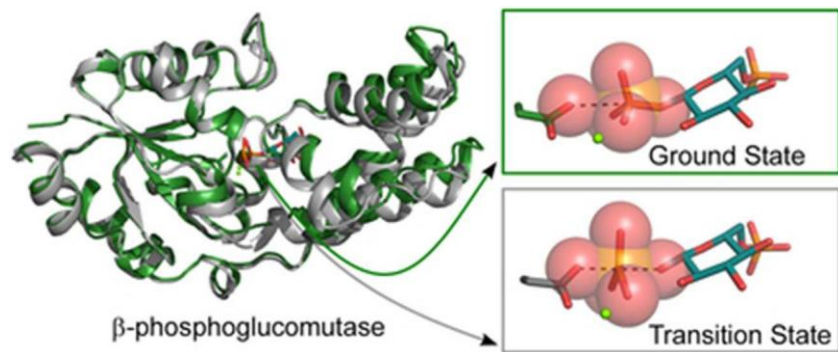
105x63mm (300 x 300 DPI)





42x20mm (300 x 300 DPI)

1  
2  
3  
4  
5  
6  
7  
8  
9  
10  
11  
12  
13  
14  
15  
16  
17  
18  
19  
20  
21  
22  
23  
24  
25  
26  
27  
28  
29  
30  
31  
32  
33  
34  
35  
36  
37  
38  
39  
40  
41  
42  
43  
44  
45  
46  
47  
48  
49  
50  
51  
52  
53  
54  
55  
56  
57  
58  
59  
60



35x14mm (300 x 300 DPI)